Faculdade de Engenharia da Universidade do Porto

Influence of Moisture Absorption on Quasi-Static and Long-Term Failure of a GRP Pipe under Lateral Compression

A dissertation by

Alcides Correia Martins de Sá

Submitted to Faculdade de Engenharia da Universidade do Porto in partial fulfilment of the requirement for the degree of Master of Science in Mechanical Engineering – Structural analysis

Supervisor: Professor Rui Jorge Sousa Costa de Miranda Guedes

Porto, April 2007

Abstract

The use of fibre reinforced polymer matrix composites in pressure retaining structures such as pressure vessels and piping systems has been confined mostly to low pressure applications when no internal liner is used. The reason for this limited use is mainly due to the uncertainty with respect to the long-term reliability of polymer matrix composites under natural environment (moisture and temperature) and multi-axial loading.

This work involves an experimental and numerical investigation of the influence of moisture on quasi-static and long-term failure of GRP pipes submitted to lateral compression. Several mechanical tests, like three-point bending and double cantilever beam were performed on unconditioned and preconditioned specimens machined from GRP pipes. Thereafter, the flexural properties and critical energy release rate for delamination (G_{Id}) of the GRP pipes were determined and the influence of moisture on its values was assessed.

Long-term modulus predictions were performed applying Time-Temperature Superposition Principle (TTSP) and an empirical power law to Dynamic-Mechanical-Thermal Analyzer (DMTA) data of unconditioned and preconditioned specimens machined from GRP pipes. The predictions were compared with the results measured on real-time creep data.

Through the short and long-term experimental data the rupture energies and strain at failure of GRP pipes were determined and compared. The measured mechanical properties were used as input data on a numerical model developed by Faria [1] which allows the study of the damage mechanisms and global mechanics of the GRP pipes. The influence of the preconditioning in moisture and loading conditions on GRP pipes failure behaviour was assessed.

Keywords

GRP pipes, Mechanical Tests; Failure; Long-Term Properties; Creep.

Resumo

O uso de materiais poliméricos reforçados com fibra de vidro (PRFV) em estruturas sob pressão, tais como reservatórios e tubagens tem sido limitado a sistemas de baixa pressão quando não é utilizado nenhum "liner" interior. Este uso limitado é devido, essencialmente, ao desconhecimento das propriedades mecânicas a longo prazo deste tipo de materiais especialmente quando são aplicados em ambientes húmidos.

Neste trabalho é feito um estudo numérico/experimental sobre a influência da humidade na rotura a curto e a longo prazo de tubagens em plástico reforçado com fibra de vidro submetidas a compressão anelar. Diversos ensaios experimentais, tais como flexão em três pontos e ensaios DCB ("Double Cantilever Beam"), foram executados em provetes (condicionados e não condicionados) previamente maquinados de tubagens em PRFV. Assim, as propriedades mecânicas à flexão e a taxa crítica de libertação de energia em delaminagem (G_{Id}) de tubagens em PRFV foram determinadas e a influência da humidade nesses valores foi estudada.

Previsões de módulo a longo prazo foram executadas aplicando o PSTT (Princípio de Sobreposição Tempo-Temperatura) e uma relação empírica sob a forma de potência a resultados de ensaios DMTA (Dynamic-Mechanic-Thermal Analyser) realizados em provetes não condicionados e pré-condicionados maquinados de tubagens em PRFV. As previsões de rigidez obtidas foram comparadas com resultados experimentais de fluência [1].

Através dos resultados de ensaios de curta e longa duração as energias e a deformação à rotura de tubagens em PRFV foram determinadas e comparadas. As propriedades mecânicas previamente determinadas foram utilizadas como parâmetros de entrada num modelo numérico desenvolvido por Faria [1] que permite o estudo dos mecanismos de dano neste tipo de estrutura. A influência do pré-condicionamento e das condições de carga na rotura das tubagens foi estudada.

Palavras-chave

Tubagens em PRFV; Ensaios mecânicos; Rotura; Propriedades a longo prazo; Fluência;

Acknowledgments

To Professor Rui Miranda Guedes my recognition goes, of course, for the total availability and capacity demonstrated in the advising and orientation of this work, but, over all, it goes for the notable easiness with which he had provided me months of pleasant joint work.

I would like to thank to Professor Marcelo Moura for the support provided on the DCB experimental tests and numerical simulations.

The experimental tasks presented in this study were carried out in the Laboratory of Mechanical Tests at INEGI/UMEC with the precious help of lab technicians. I would like to thank to Eng. º Hugo Faria, who preceded me in this study, for the availability and cooperation in the present work. I would also like to thank to Dr. Paulo Nóvoa for his support and advices in the experimental work.

I have to enhance the good work environment which Unidade de Materiais e Estruturas Compósitas of INEGI received me with. I cannot leave without thank to the unit's direction, Professor Torres Marques and Dr. Nuno Correia, the availability, efficient advises and the freedom I was transmitted for the best prosecution of the study.

Agradecimentos

Ao Professor Rui Miranda Guedes o meu reconhecimento vai, naturalmente, para a total disponibilidade e capacidade demonstradas no aconselhamento e orientação deste trabalho, mas, sobretudo, para a notável facilidade com que me proporcionou meses de agradável trabalho em conjunto.

Gostaria de agradecer ao Professor Marcelo Moura o apoio prestado nos ensaios experimentais DCB e respectivas simulações numéricas.

As tarefas experimentais apresentadas neste estudo foram realizadas no Laboratório de Ensaios Mecânicos do INEGI/UMEC cujos equipamentos e recursos humanos foram imprescindíveis. Gostava de agradecer ao Eng.º Hugo Faria, que me antecedeu neste estudo a disponibilidade e cooperação demonstradas no decorrer do trabalho. Também gostava de agradecer ao Dr. Paulo Nóvoa o apoio e conselhos fornecidos no decorrer do trabalho experimental.

Devo também realçar o bom ambiente de trabalho com que a Unidade de Materiais e Estruturas Compósitas do INEGI me acolheu. Não posso deixar de agradecer à direcção dessa mesma Unidade, Professor Torres Marques e Dr. Nuno Correia, a disponibilidade, os conselhos e a liberdade que me foram transmitidos para a melhor prossecução do trabalho.

Table of Contents

1. Introduction

In recent years materials that possess high specific strength and specific modulus were developed to fulfil the need for advanced lightweight structures. Fibre reinforced plastics (FRP) are materials that have these properties, and are being used in structures as primary as well as secondary load carrying members.

Laminated FRP structures assume a specific behaviour due, not only to the mechanical properties of their components but also to the imposed geometry to each ply in the laminate. Generally the reinforcement fibres have better elastic properties than the polymeric matrix. Hence, the global properties of the composite structures depend mostly of the reinforcement properties [1]. However, quantifying those global properties isn't as simple as it appears. In terms of initial mechanical performance of the assembled materials, the four main factors governing the fibres contribution are the basic physical properties of the fibres, the quality of the fibre-matrix interface and the volume, the geometry and the orientation of the fibres in the composite [1].

Polymer matrix composite materials offer many superior properties in comparison with other materials, among them, high strength to weight ratio, superior corrosion resistance and the ability to tailor the material system to a particular requirement. GRP (glass reinforced polymer) pipes are an alternative to traditional pipes in metallic materials where corrosion, weight and environmental effects limit their use. In piping systems, GRP pipes have been increasingly introduced and are now an important class of engineering structures.

The use of fibre reinforced polymer matrix composites in pressure retaining structures such as pressure vessels and piping systems has been confined mostly to low pressure applications when no internal liner is used. The reason for this limited use is mainly due to the uncertainty with respect to the long-term reliability of polymer matrix composites under natural environment (moisture and temperature) and multi-axial loading. These types of pipes are frequently subjected to humid conditions and it is widely recognized that these materials absorb moisture from the environment and that moisture has an important influence on its mechanical properties [2-4]. Environmental factors are of extreme importance with respect to the service life of composite components based on polymeric engineering materials [4]. It is very important to know

the behaviour of polymer matrix composites when exposed to humid environments in order to predict their long-term properties. Complex phenomena like plasticization of the matrix, debonding, rearrangement of the chemical structure and relaxation can occur on fibre reinforced polymer composites when they are exposed to moisture [3, 5-8]. The strength of bonding at the fibre-matrix interface has also been shown to degrade in the presence of temperature and moisture. It has been hypothesized that rather than diffusing through the matrix (a slow and temperature dependent process) moisture will diffuse with more ease along the fibres and destroy the bond at the fibre-matrix interface which plays a pivotal role in composite strength by load transfer [9]. Without a strong bond at the interface, the properties of the weakest link, the matrix, will dominate for most cases of fibre reinforcement.

The main goals of this work are to study the influence of moisture on the failure behaviour of GRP pipes submitted to quasi-static and long-term compressive ring loads.

Three-point bending tests and Double Cantilever Beam (DCB) tests were performed on unconditioned and preconditioned specimens machined from GRP pipes in order to determine the influence of moisture on its flexural properties and critical energy release rate for delamination (G_{Id}). A moisture diffusion analysis was also done in order to study the applicability of Fick's second law to the moisture diffusion process of this kind of material.

DMTA (Dynamic-Mechanic-Thermal Analysis) tests were performed on circumferential specimens machined from GRP pipes. TTSP (Time-Temperature Superposition Principle) and an empirical power extrapolation method were applied to DMTA data in order to perform long-term predictions of the circumferential modulus of the studied GRP pipes. The experimental data of creep tests performed by Faria [1] was treated in order to obtain the variation of the GRP pipes modulus occurred during the experimental tests. The DMTA predictions were compared with the results obtained on real-time creep tests. The analysis of the DMTA data of specimens conditioned in different environments enabled the study of the hygrothermal effects on the instantaneous modulus and viscoelasticity of the material.

Through the short and long-term experimental data the GRP pipes rupture energy and strain at failure was determined and compared. The influence of the preconditioning and loading scheme on failure of GRP pipes was assessed. The determined flexural properties and G_{Id} for unconditioned and preconditioned state were used as input data on

a numerical model developed by Faria [1] in order to study the influence of its variation on damage mechanisms and global mechanics of the analysed GRP pipes.

2. Influence of moisture absorption on flexural properties of GRP pipes

2.1. Introduction

In this section is described the work done to study the influence of moisture absorption on flexural properties of the analysed GRP pipes.

As it was mentioned on Section 1, environmental factors are of extreme importance with respect to the service life of composite components based on polymeric engineering materials. It is very important to know the behaviour of polymer matrix composites when exposed to humid environments in order to predict their long-term properties.

In order to predict the effects of moisture and moisture gradient in these kinds of materials their moisture diffusion rate (diffusivity) must be known.

Moisture absorption by the resin-matrix composites can take place by capillarity action along the fibre/matrix interface, through cracks or voids in the resin, and diffusion through the matrix [5, 10-11].

Numerous diffusion models have been proposed over the years for modelling hygrothermal effects in polymers and in FRP. The first diffusion model was proposed by Fick by analogy with the heat conduction model [5, 11-13]. Most of the studies of water absorption made in composites rely on Fick´s second law that writes [5]:

$$\frac{\delta c}{\delta t} = D_3 \frac{\delta^2 c}{\delta x_3^2} \tag{1}$$

where c represents the moisture concentration and D_3 the moisture diffusion coefficient in the through thickness direction, supposed to be independent of the spatial and temporal coordinates [12]. Equation 1 describes the free reversible diffusion of molecules of water driven only by concentration gradients [12].

The diffusion of moisture in a material is said to be Fickian when [5]:

- In the beginning of the phenomenon the absorption curve is linear;
- Next to the linear part of the phenomenon the curves show a concave behaviour asymptotically tending to a state of equilibrium;
- The absorption and desorption curves are coincident;
- The absorption curves for different environmental conditions are coincident;

It is well known that the behaviour of materials in moist environment depends greatly on the environmental conditions and on the properties of the material [5, 11-12, 14]. Some materials in an environment with constant humidity but varying temperatures show the same level of absorbed moisture and different rate of absorption [5, 14] but in other ones the level of absorbed moisture also shows variations with different temperatures [12]. In the reverse case (constant temperature but varying amounts of humidity) there are materials where the rate of absorption stays constant and the level of absorbed moisture increases with an increase in the ambient humidity [5, 14], and there are cases in which the rate of absorption also increases with an increase in ambient humidity [12].

Specimen's thickness also has a pronounced effect on the moisture diffusion rate. Thinner specimens reach equilibrium faster than the thicker ones [5, 12, 15].

Shen and Springer [11] showed that a unidirectional composite material takes moisture faster in the direction parallel to the fibres than in the perpendicular direction. This is due to the quality of the resin-fibre interface [14]. So, the edge effect should be taken into account when calculating the moisture diffusion coefficients.

In some composites Fickian model is able to describe the initial stages of the diffusion process, but unable to describe the whole phenomenon. This model tends to overestimate the rate of absorption especially for intermediate exposure times, and is unable to account for changes to the polymer induced by the absorbed moisture, such as relaxation (swelling), dissolution, chemical degradation or induced damage [3, 5-6, 14, 16-18].

Many researcher's proposed models to describe the whole phenomenon of moisture absorption. Some of them have suggested that the deviations from the Fick's model can be explained by a two stage Fickian model and others claim that the diffusion is non Fickian [13, 16-17]. The applicability of Fick´s law for a given material can't be guessed a priori and must be determined from moisture

absorption/desorption test data [5, 16]. Roy [16] proposed a model that allows the characterization of non-Fickian diffusion coefficients in order to predict moisture weight gain data for a polymer below its T_g. Maggana [17] uses the Jacobs-Jones model which considers a two-phase system consisting of a master phase (where the major part of the water is absorbed), which is homogeneous and non-polar, and of a second phase with different density and hydrophilic character.

The influence of moisture on flexural properties of several FRP materials has been studied by many researchers [2-5, 7, 9, 19-20].

Nishizaki [2] performed three-point bending tests on preconditioned and unconditioned pultruded glass fibre (E-glass) reinforced polymer (vinyl ester). The bending strengths of the GFRP specimens dropped compared to initial bending strength values. Specimens immersed at the 60ºC condition exhibited greater declines in bending strength compared to specimens in an atmosphere at 60ºC or an immersion at 40ºC.

Perreux [3] studied the influence of moisture on the mechanical properties and kinetics of damage in glass/epoxy composite pipes manufactured by the filament winding technique. The influence of ageing was characterized by experiments carried out on specimens subjected to various hygrothermal treatments at 60ºC. A large scatter was obtained but it was concluded that the rigidity of the composite remains almost constant during ageing time.

Kootsookos [8] assessed the influence of seawater on the mechanical properties of glass/polyester and glass/vinyl. The specimens were immersed in a marine environment and tested at several intervals of time. The obtained results show a considerable scatter in the flexural properties of the polyester-based composites. However, the flexural modulus values are on average 10-20% lower than the original modulus, indicating some small deterioration on the stiffness caused by the seawater. Despite the scatter there is a general reduction in the flexural strength of the polyester composites, and at the saturation time the strength has degraded by 20-40%. The change to the flexural properties with immersion time is more obvious for the vinyl ester based composites, where the amount of scatter is lower. The flexural modulus decreased about 30% and the strength was reduced for about 40-50%.

Ellyin [9] assessed the effects of moisture absorption and exposure to elevated temperature on mechanical properties of glass fibre reinforced epoxy composite pipes by performing multi-axial tests on unconditioned and preconditioned

specimens. The immersion in water at 50ºC caused a decrease in the stress and strain at failure for the pure axially and pure hoop loaded specimens in comparison with the values obtained on the specimens conditioned in water at 20ºC. The values of the initial elastic modulus in the fibre dominated direction (hoop direction) aren't affected by the immersion in water at 20 and at 50ºC. In contrast, in the matrix dominated direction (axial direction) there is a decrease in the elastic modulus due to the water absorption of the matrix.

Akay [20] studied the absorption behaviour and the influence of moisture on the thermal and mechanical properties of Kevlar/epoxy resin laminates and showed that moisture doesn't influence the elastic modulus but has a negative influence on the flexural strength.

In this section the effects moisture on the flexural modulus and ultimate flexural strength of the analysed GRP pipes were studied by performing three-point bending tests on unconditioned and preconditioned specimens machined from the circumferential and longitudinal direction of the pipes. Due to the curved geometry of the specimens a new data reduction scheme was proposed and compared with the one used for linear beams using the finite element method. A moisture diffusion analysis was also performed allowing the study of the applicability of the Fick's second law to the moisture diffusion process of this kind of material. The maximum moisture content absorbed by the material and the through thickness diffusion coefficients was determined.

2.2. Specimens

The specimens were cut-out from GRP pipes made by filament winding. The pipes and the machined samples are depicted in Figure 1.

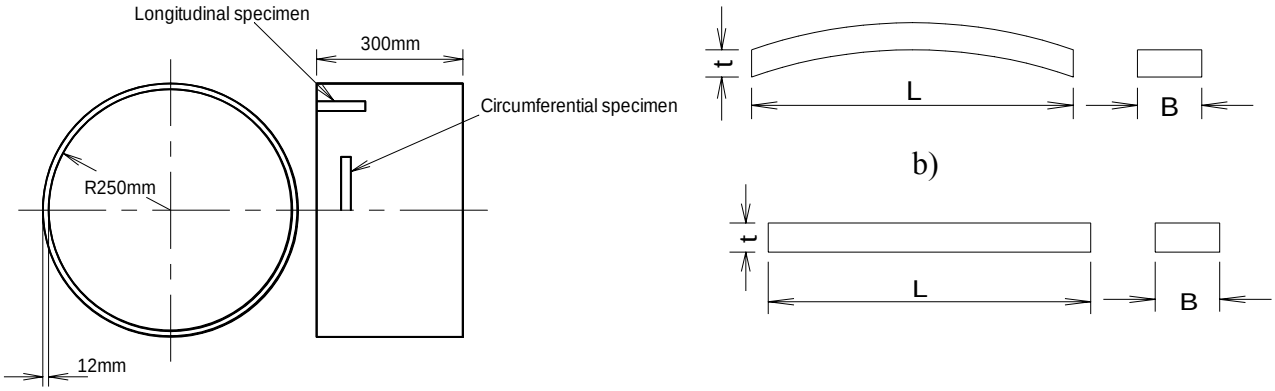

a) c)

Figure 1 – a) Pipe and cut specimen; b) Circumferential specimen; c) Longitudinal specimen.

The pipes were made of polyester with fibreglass coiled at 90º and charges (almost composed by sand). Burn-off tests, described on Section 4.2, showed that these pipes contains about 36% of resin, 41% of sand and 23% of fibre. The manufacturer claims that the pipe wall is made up of three different major layers, each one possessing different properties according to its functions. Accordingly the pipe wall is composed by an inner layer which provides the chemical resistance, by a mechanical resistant layer, and a top coat. The mechanical properties of the pipes supplied by the manufacturer are given in Table I.

Table I – Properties of the pipes supplied by the manufacturer.

E_c (GPa)	E_r (GPa)	E_L (GPa)
10.547	3.808	3.808

In Table I the subscript *c* means circumferential direction, *r* means radial direction and *L* means longitudinal direction.

Thirty specimens were machined from the circumferential direction and fifteen specimens were machined from the longitudinal direction of the GRP pipes according to the dimensions proposed on standard ISO 14125 [21]. The width of the specimens didn't respect the one proposed on standard ISO 14125 [21] in order to

minimize the border effects on the water diffusion analysis also performed on these specimens.

Ten circumferential and five longitudinal specimens were soaked in water at room temperature (≈15ºC) until they reached saturation. Ten circumferential and five longitudinal were soaked in water at 50ºC until they reached saturation. The average dimensions of the tested specimens are described on Table II.

Table II – Average dimensions of the tested specimens.

Specimen	***t* (mm)**	***B* (mm)**	***L* (mm)**
Circumferential	12.0	61.9	247.9
Longitudinal	11.8	62.1	239.9

2.3. Experiments

2.3.1. Moisture diffusion tests

The specimens were conditioned in water at room temperature and in water at 50ºC in two vessels as depicted in Figure 2.

a) b)

Figure 2 – a) Samples conditioned at room temperature; b) Samples conditioned at 50ºC;

One of the vessels was equipped with a 2KW electrical resistance in order to maintain the temperature of the water at 50ºC.

All the specimens were periodically removed from the conditioning chambers (twice a day on the first 400 hours of conditioning and once a day on the remaining hours) and after being carefully wiped out their weight was controlled in a KERN® digital scale with a resolution of 0.1g in order to determine the moment when saturation was reached.

2.3.2. Flexural tests

The circumferential and the longitudinal samples were tested in three-point bending following the standard procedure ISO 14125 [21] in a universal INSTRON machine where the load/displacement data was recorded. The span of the device was 16 times the thickness of the specimen and the speed of testing was 2/5 of the thickness.

Five unconditioned circumferential specimens, five circumferential specimens saturated in water at room temperature and five circumferential specimens saturated in water at 50ºC were tested according to the scheme presented in Figure 3a (concave side down). Five unconditioned circumferential specimens, five circumferential specimens saturated with water at room temperature and five circumferential specimens saturated with water at 50ºC were tested according to the scheme presented in Figure 3b (concave side up).

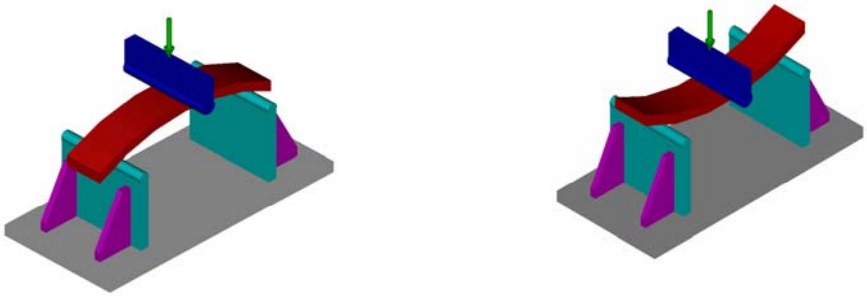

a) b)

Figure 3 – a) Inside layer subjected to tensile stress; b) Inside layer subjected to compressive stress.

2.4. Data reduction schemes

2.4.1. Moisture diffusion tests

The Fick´s second law is given by Equation 1.

For a plate of infinite dimensions, the boundary conditions are:

$$\begin{cases} c = c_i & \text{if} \quad 0 \le x_3 \le e;\ t < 0 \\ c = c_\infty & \text{if} \quad x_3 < 0;\ x_3 > e;\ t \ge 0 \end{cases} \tag{2}$$

where c_i and c_∞ are respectively the initial and saturated moisture concentrations, e is the plate thickness and t is the time.

The solution to this problem can be expressed as [12]:

$$\frac{c_t - c_i}{c_\infty - c_i} = 1 - \frac{4}{\pi}\sum_{j=0}^{\infty}\frac{1}{(2j+1)^2}\sin\left(\frac{(2j+1)\pi x_3}{e}\right)\exp\left(-\frac{(2j+1)^2\pi^2 D_3 t}{e^2}\right) \tag{3}.$$

With Equation 3 the moisture concentration profiles through the thickness at any time can be calculated.

By integrating Equation 3 with respect to the space variable, it is possible to derive the total mass of water absorbed by this infinite plate at time t [12]:

$$\frac{m_t - m_i}{m_e - m_i} = \frac{M_t}{M_e} = 1 - \frac{8}{\pi^2}\sum_{j=0}^{\infty}\frac{\exp\left(-\frac{(2j+1)^2\pi^2 D_3 t}{e^2}\right)}{(2j+1)^2} \tag{4}$$

where m_t is the mass of the specimen at time t, m_i is the initial mass of the specimen and m_e is the mass of the specimen when it reaches saturation.

From Equation 4 it can be seen that $\frac{M_t}{M_e}$ is a linear function of $\frac{\sqrt{t}}{e}$ up to a given $\frac{\sqrt{t}}{e}$ value as it is illustrated in Figure 4 [5].

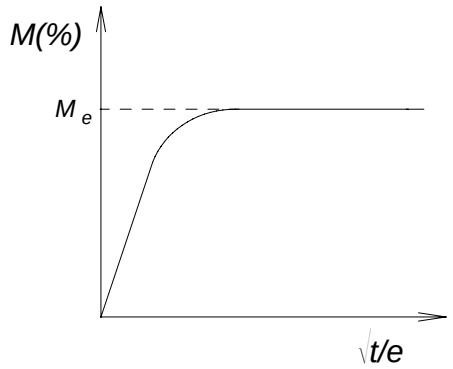

Figure 4 – Fickian absorption curve.

The absorption curve is used to determine M_e and the slope is recorded. Then D_3 can be calculated using [5]:

$$D_3 = \frac{\pi S^2}{4M_e^2} \tag{5}$$

where S is the slope of the linear part of Equation 4.

Studies made by Morais [5] showed that a good approximation (error less than 0.1%) for the series presented in Equation 4, which describes the one-dimensional Fick's model, is obtained using:

$$\begin{cases} \dfrac{M(t)}{M_e} = \dfrac{2}{\sqrt{\pi}}\sqrt{T_3} & \text{if} \quad \sqrt{T_3} \le 0.45 \\ \dfrac{M(t)}{M_e} = 1 - \dfrac{8}{\pi^2}\exp\left(-\dfrac{\pi^2 T_3}{4}\right) & \text{if} \quad \sqrt{T_3} > 0.45 \\ T_3 = \dfrac{D_3 t}{e^2} \end{cases} \tag{6}.$$

2.4.2. Flexural tests

Two different data reduction schemes were applied to the experimental data of the flexural tests. The experimental data of the three-point bending tests of the longitudinal specimens was treated according to the standard procedure ISO 14125 [21].

The data reduction scheme presented on ISO 14125 [21] for linear beams might induce considerable deviations on the results when applied to the experimental data of curved beams. So, for the analysis of the experimental data of the circumferential specimens a new method, based on thin curved beam theory, was proposed (Annex 1) and compared with the one presented on the standard procedure ISO 14125 [21] using the finite element method (Annex 2).

2.4.2.1. Data reduction scheme presented on ISO 14125

Using the P-δ curves obtained on the universal INSTRON machine the values of flexural modulus of elasticity and ultimate flexural stress are obtained using:

$$E_f = \frac{l_0^3}{4Bt^3}\frac{\Delta F}{\Delta y} \tag{7}$$

$$\sigma_f = \frac{3F_{\max}l_0}{2Bt^2} \tag{8}$$

where E_f is the flexural modulus of elasticity, σ_f is the ultimate flexural stress, l_0 is the test span, B is the width of the specimen, t is the thickness of the specimen, $\frac{\Delta F}{\Delta y}$ is the slope of the linear part of the experimental P-δ curve and F_{max} is the load at rupture.

This data reduction scheme was applied on the computation of the modulus of elasticity and ultimate flexural stress of the longitudinal specimens.

2.4.2.2. Data reduction scheme based on thin curved beam theory (TCBT)

The flexural modulus of elasticity and the ultimate flexural stress of the curved specimens are given by:

$$E_f = -\frac{1}{4}\frac{R_m.\left(\beta - sen\left(\beta\right)cos\left(\beta\right)\right)}{cos\left(\beta\right)^2.B.\left(-R_m.ln\left(-\frac{2R_m+t}{-2R_m+t}\right)+t\right)}\frac{\Delta F}{\Delta y} \tag{10}$$

$$\sigma_f = \frac{1}{2}\frac{F_{max}.sen\left(\beta\right)y}{cos\left(\beta\right).B.\left(-R_m\,ln\left(-\frac{2R_m+t}{-2R_m+t}\right)+t\right).\left(R_m+y\right)} \tag{11}$$

where E_f is the flexural modulus of elasticity, σ_f is the ultimate flexural stress, $\frac{\Delta F}{\Delta y}$ is the slope of the linear part of the *P*-δ curve, B is the width, R_m is the medium radius of the pipe, t is the thickness of the specimen, F_{max} is the load at rupture, y is the distance from the neutral axis to the point where σ_f is to be determined and β is the angle between the support and the point where the load is applied (Figure 5).

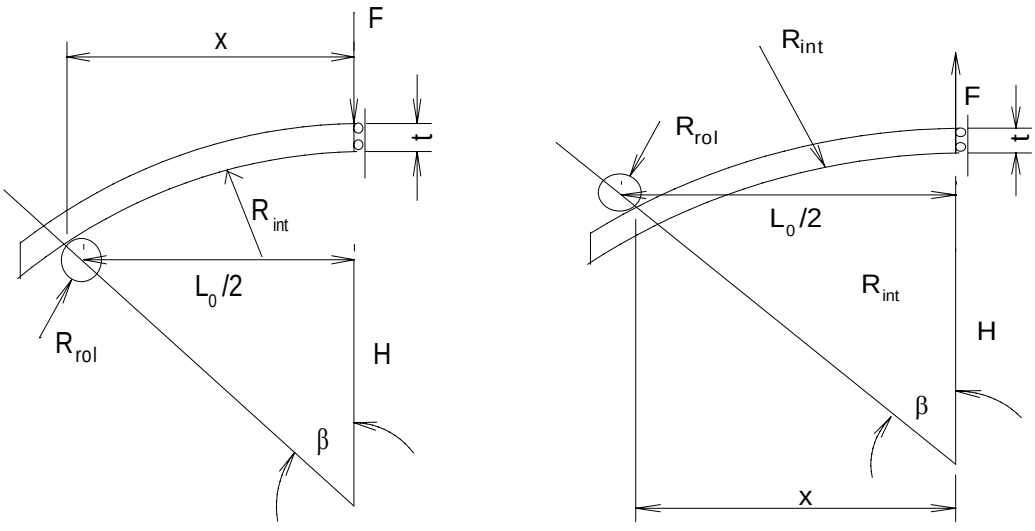

a) b)

Figure 5 – a) Specimen tested with the concave side down; b) Specimen tested with the concave side up.

The value of β is different when the specimens are tested with the concave side up or down (Figure 5). In the specimens tested with the concave side down, β is given by:

$$H = \sqrt{\left(R_i - R_{rol}\right)^2 - \frac{L_0^2}{4}} \tag{12}$$

$$\beta = a\tan\left(\frac{L}{2H}\right) \tag{13}.$$

In the specimens tested with the concave side up β is given by:

$$H = \sqrt{\left(R_{ext} + R_{rol}\right)^2 - \frac{L_0^2}{4}} \tag{14}$$

$$\beta = a\tan\left(\frac{L}{2H}\right) \tag{15}.$$

The TCBT was used on the computation of the modulus of elasticity and ultimate flexural stress of circumferential specimens (Annex 2).

2.5. Results

2.5.1. Moisture diffusion tests

The obtained absorption curves $\left(M(\%) = f\left(\sqrt{t}\right)\right)$ are depicted in Figures 6-8 with:

$$M(\%) = \frac{M(t) - M_i}{M_i} \times 100 \tag{16},$$

where *M(t)* is the mass of the specimen at time *t*, M_i is the initial mass of the specimen and *M(%)* is the total mass content of water in the specimens at time *t*.

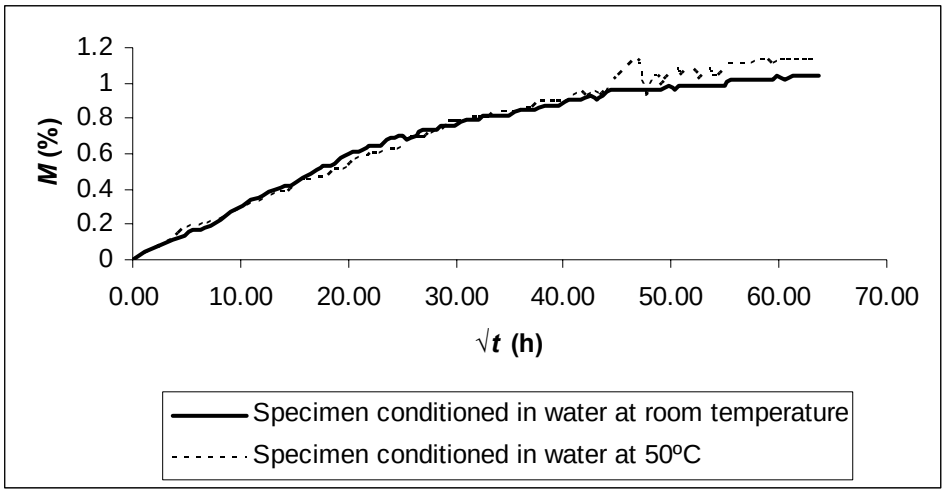

Figure 6 – Comparison of the absorption curves of two specimens conditioned on the two different environments.

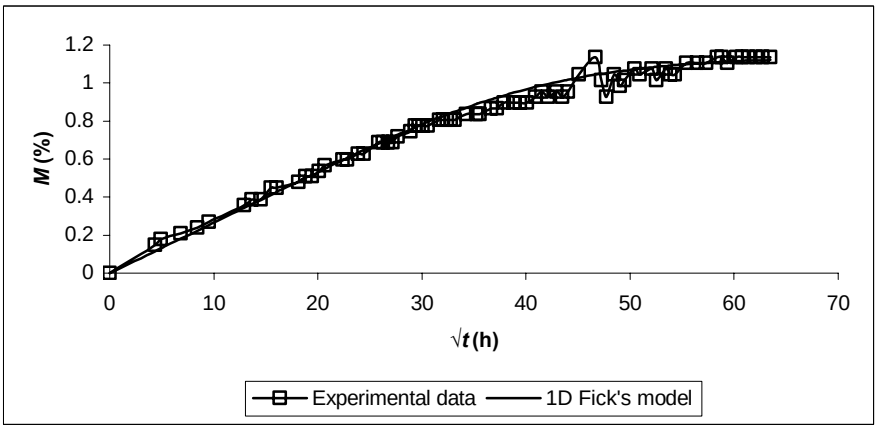

Figure 7 – Fitting the Fickian model to the experimental data of a specimen conditioned in water at 50ºC.

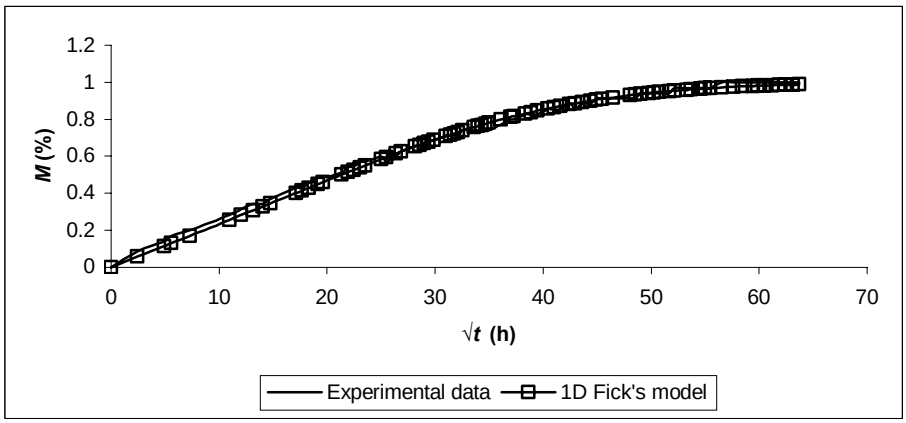

Figure 8 – Fitting the Fickian model to the experimental data of a specimen conditioned in water at room temperature.

Some specimens were excluded from the diffusion analysis because during the tests they lost part of their top coat.

In the absorption curves of the specimens conditioned at 50ºC it appears an elbow in the curves when $45<\sqrt{t}<48$. This was due to some problems which occurred with the heating resistance at this time of the experimental program.

The maximum mass content and the through thickness diffusion coefficients of the specimens are given on Table III.

Table III – Maximum mass content and trough thickness diffusion coefficient of the specimens.

Conditioning	**Specimen**	**Maximum mass content (%)**		**Through thickness diffusion coefficient (mm^2/h)**	
		Average	**St. Dev.**	**Average**	**St. Dev.**
Water at room temperature	**Circumferential**	1.011	0.025	0.073	0.016
	Longitudinal	1.019	0.051	0.069	0.016
Water at 50ºC	**Circumferential**	1.075	0.042	0.068	0.016
	Longitudinal	1.066	0.025	0.066	0.0048

2.5.2. Flexural tests

Some of the obtained experimental *P-δ* curves are depicted in Figure 9.

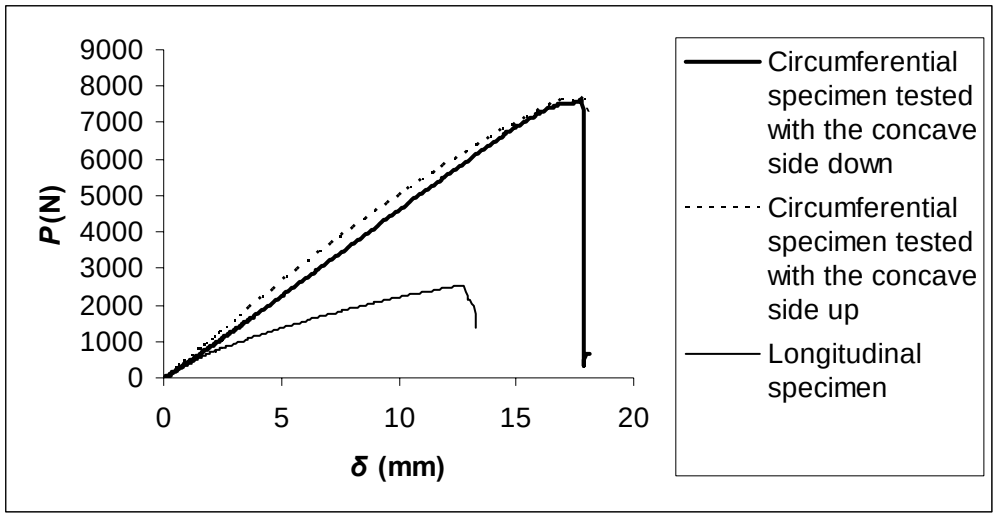

Figure 9 – *P*-δ curves of some unconditioned specimens.

The experimental results obtained for the unconditioned and preconditioned specimens are depicted on Tables IV and V.

Table IV – Influence of moisture on flexural modulus of the analysed GRP pipes.

E_c (GPa) of circumferential specimens tested with the concave side down			
Conditioning	**Average**	**St. dev.**	**Variation (%)**
Unconditioned	11.212	0.686	-
Water at room temperature	11.207	0.339	0%
Water at 50ºC	10.082	0.795	-10%
E_c (GPa) of circumferential specimens tested with the concave side up			
Conditioning	**Average**	**St. dev.**	**Variation (%)**
Unconditioned	10.275	0.804	-
Water at room temperature	9.465	0.72	-7.8%
Water at 50ºC	8.817	0.474	-14.2%
E_L (GPa) of longitudinal specimens			
Conditioning	**Average**	**St. dev.**	**Variation (%)**
Unconditioned	6.09	0.337	-
Water at room temperature	5.635	0.345	-7.4%
Water at 50ºC	4.273	0.337	-29.8%

Table V – Influence of moisture on ultimate flexural strength of the analysed GRP pipes.

σ_R (MPa) of circumferential specimens tested with the concave side down			
Conditioning	**Average**	**St. dev.**	**Variation (%)**
Unconditioned	249.46	20.29	-
Water at room temperature	267.92	12.13	+7.4%
Water at 50ºC	224.35	14.45	-10.0%
σ_R (MPa) of circumferential specimens tested with the concave side up			
Conditioning	**Average**	**St. dev.**	**Variation (%)**
Unconditioned	245.56	12.71	-
Water at room temperature	223.96	11.46	-8.79%
Water at 50ºC	202.88	9.26	-17.38%
σ_R (MPa) of longitudinal specimens			
Conditioning	**Average**	**St. dev.**	**Variation (%)**
Unconditioned	85.19	9.25	-
Water at room temperature	99.57	6.1	+16.9%
Water at 50ºC	81.02	7.34	-4.9%

2.6. Discussion of results

2.6.1. Moisture diffusion tests

Some scatter was observed on moisture diffusion tests. This fact can be explained by the differences of voids on the different specimens because they were removed from different regions of the pipe wall.

There are no big differences on maximum mass content and through thickness diffusion coefficients between the specimens conditioned in water at ambient temperature and the ones conditioned in water at 50ºC.

In Figures 7 and 8 it is seen that the one-dimensional Fick model fits very well the experimental data and is able to predict the moisture absorption phenomenon in this kind of material at the two different environments tested (ambient temperature and 50ºC). Yet, one can not say for sure that the

phenomenon of moisture diffusion in this material is really Fickian because only the absorption phenomenon was studied.

The maximum water content absorbed by the circumferential and longitudinal specimens is about 1.04% and the moisture diffusion coefficients are approximately 0.07 mm^2/h. These specimens took about 3000 hours to reach saturation on both conditioning cases. On these specimens the water temperature doesn't induce considerable differences on the absorption process.

2.6.2. Flexural tests

High scatter of flexural modulus and ultimate flexural strength was obtained. This phenomenon can be related with several factors, among them, the complex heterogeneous structure of the pipe wall and to some initial distortion of the specimens which provide a deficient support of the specimens on the support rollers.

On Tables IV and V, it is seen that the saturation of the specimens with moisture at room temperature have a negligible effect on the flexural modulus and on the ultimate flexural strength on the circumferential and longitudinal direction. On the circumferential specimens saturated in water at 50ºC it is seen a lowering (about 12%) on the values of flexural modulus and ultimate flexural strength. However due to the high scatter measured one cannot say that the saturation in water at 50ºC promotes significant reductions on the values of flexural properties on the circumferential direction. In the longitudinal direction the value of flexural modulus of the pipe suffer a decay of about 30% when saturated in water at 50ºC.

2.7. Conclusions

Water absorption tests until saturation were performed on specimens machined from GRP pipes. The one-dimensional Fick model is quite reliable to predict the characteristics of moisture absorption of this kind of material in the tested environments. The maximum water content absorbed by the circumferential and longitudinal specimens was about 1.04% and the moisture diffusion coefficient was

approximately 0.07 mm^2/h. The higher preconditioning temperature didn't accelerate the time to saturation, i.e. the saturation times were similar for room temperature and 50ºC (about 3000 hours).

After reach saturation the specimens were tested in flexure in order to assess the influence of the absorbed moisture on the flexural modulus and ultimate flexural strength. A reliable method based on thin curved beam theory for analysing curved beams subjected to three-point bending was developed. A high scatter was obtained. The conditioning on the two different environments doesn't have a significant influence on the flexural properties in the circumferential direction. The conditioning in water at 50ºC promotes a 30% decrease of flexural modulus in the longitudinal direction.

3. Influence of moisture absorption on critical strain energy release rate in mode I for delamination (G_{Id}) of GRP pipes

3.1. Introduction

The critical energy release rate for delamination G_{Id} of GRP pipes as well as the influence of moisture on its values was studied and determined. The description of the work developed follows.

The studied GRP pipes are normally subjected to diversified mechanical requests and it's important to know the influence of interlaminar and intralaminar defects in structural integrity of this kind of structures. Delamination may occur as a result of contaminations during lay-up, accumulation of voids during processing, shock or blast loading, or hard object impact loading during service life of the structure [22].

Some studies have been performed in order to characterize mode II [23] and mixed mode [22] delamination crack growth in specimens cut-out from GRP pipes in longitudinal direction. No studies were found related with specimens cut-out from circumferential direction in order to characterize mode I, II or mixed mode.

The influence of moisture on the critical energy release rate (G_{Ic}) values of several materials has been studied by many researchers [8, 24-29].

Srivastava [24] presented an experimental programme for the study of the effects of moisture on mode I and mode II interlaminar fracture toughness of aluminium tri-hydrate and polyethylene filled and unfilled quasi-isotropic glass fibre reinforced epoxy-vinylester resin composites. The specimens were exposed in water at room temperature for a period of 8 months and the effect of moisture content on the values of G_{Ic} and G_{IIc} were obtained at every 2 months. The obtained results showed that water immersion promoted an increase on the measured mode I fracture toughness.

Zenasni [25] determined experimentally the hygrothermal effects on the mode I and mode II critical energy release rates using the corrected beam theory on two

types of woven (2/2 Twill, 8-Harness Satin) glass fibre and 8-Harness Satin carbon fibre. The matrix was polyetherimide. The results showed that the delamination energy suffered a smaller loss with time of aging in the 8-Harness Satin fabric than in the 2/2 Twill. Moreover, delamination energy decreased with exposure time when the reinforcement was made with glass fibre rather than with carbon fibre. In mode II, the same behaviour was observed as in mode I, the 2/2 Twill arrangement was less resistant to fracture than the 8-Harness Satin, and the carbon fibre reinforcement was found to be more brittle than that of glass fibre. In both mode I and mode II, the glass fibre reinforced material in the 8-Harness Satin arrangement increased the initial resistance to delamination. The other two materials presented an important loss in critical energy from the beginning in mode I and mode II.

Khayankarn [26] studied the stability of epoxy/glass interfaces subjected to hygrothermal ageing based on a fracture mechanics approach. The adhesive strength was measured under dry, as-processed conditions and as a function of exposure time to an 85ºC/85% relative humidity environment. The strain energy release rate, G_c, dropped significantly with ageing time.

Chou [27] studied the effects of fibre orientation and moisture content on G_{Ic}/G_{IR} (Mode I energy release rate at initiation/propagation) and G_{IIc}/G_{IIR} in CFRP laminates. The interlaminar fracture toughness in several plain weave interfaces was measured using the DCB and ENF tests. For the 0/0 interface the interlaminar fracture toughness under dry, 50% and wet conditions was also measured. The degree of moisture absorption affected G_{Ic} slightly and G_{IR} strongly. G_{Ic} under dry and wet conditions is lower than that under the 50% equilibrium condition in the case of characterizing G_{Ic} at P_{NL}. Contrary to G_{Ic} characterized at P_{NL}, the fracture toughness is not affected by the moisture content in the case of characterizing G_{Ic} at P_5 and P_{MAX}. G_{IR} under the dry condition increases as the crack propagates. On the other hand, G_{IR} under the 50% equilibrium condition is almost constant during propagation. G_{IR} under the wet condition increases at the early stage of propagation, and then it becomes almost constant during propagation.

Asp [28] studied the moisture and temperature effects in mode I, mode II and mixed mode on carbon/epoxy specimens. The dry and moisturized specimens were tested at -50º, 20º and 100º. No general effect of moisture content on the critical energy release rate, G_{Ic}, was observed. Neither was temperature found to strongly

affect G_{Ic}. However, the results for HTA/6376C show a small increase in G_{Ic} at 100ºC.

Selzer [29] studied the effect of moisture on the mechanical properties and failure behaviour of fibre-reinforced polymer composites. Three materials (epoxy, modified epoxy and PEEK) were investigated, witch were all reinforced with continuous carbon fibres. The specimens were immersed in distilled water at different temperatures. After various periods of time the specimens were taken out of the baths and subjected to the mechanical tests. The G_{Ic} values of the carbon/epoxy specimens increased with increasing moisture content (to a maximum increase of 64%). The temperature at witch the specimens were soaked was found to have no influence on the fracture toughness. Mode I tests carried out on carbon/PEEK showed that the properties of this material were neither affected by the moisture content nor by the temperature at which the specimens were immersed.

Moisture and temperature affects the values of G_{Ic} in different ways. The values of G_{Ic} in some materials are negatively affected by moisture and temperature but in other cases moisture and temperature increase the values of G_{Ic} [24-29].

DCB (Double Cantilever Beam) tests was performed on unconditioned and preconditioned specimens cut-out from the circumferential direction of the pipes in order to determine its critical strain energy release rate for delamination (G_{Id}). The specimens geometry is as depicted in Figure 10.

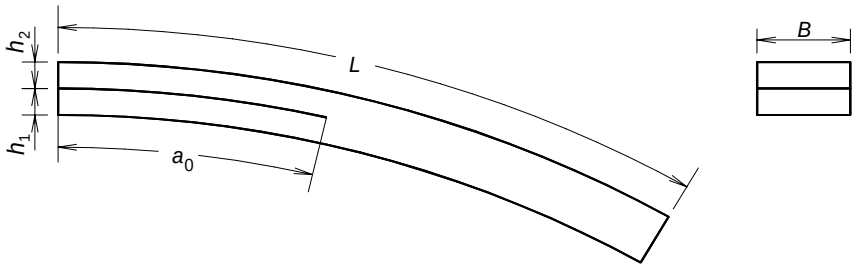

Figure 10 – Specimens geometry.

These specimens were loaded in mode I following the standard procedure described in [30]. Although these specimens were loaded in mode I, because of their geometry this becomes a mixed mode test (mode I and mode II). In order to quantify the influence of mode II on G_{Id} values a two-dimensional numerical analysis, with interface finite elements previously developed [31-32], which includes a progressive

damage model based on the indirect use of fracture mechanics, was performed. The experimentally determined G_{Id} value was introduced in the numerical model as input data. The P-δ-a data obtained numerically was used to estimate the new G_{Id} value by using different data reduction schemes. The comparison with the inputted value should validate or not the DCB tests on curved beams to obtain the critical strain energy release rate in mode I of these kinds of specimens.

3.2. Calculation of G_{Id}

In order to obtain the critical strain energy release rate in mode I for delamination (G_{Id}), different data reduction schemes were used. Some conventional methods used for linear beams are presented. However, for this special specimen, the performance of the chosen methodologies was evaluated considering the curved beam theory.

3.2.1. Data reduction schemes

Three methodologies were used to compute the G_{Id} values.

Corrected beam theory (CBT)

This method is proposed in [30], where G_{Id} is obtained from:

$$G_{\mathrm{Id}} = \frac{3P\delta}{2B\left(a+|\Delta|\right)}F\,, \tag{17}$$

where P is the load, δ is the load line displacement, B is the width of the specimen, a is the delamination crack lengths, F is the large displacement correction and Δ is a correction to the delamination crack lengths. In this method the parameters P and δ are retrieved from the P-δ curves of the experimental results and a is the length of the precrack plus the delamination crack lengths measured during the tests. The large displacement correction factor is obtained through [30]:

$$F = 1 - \frac{3}{10}\left(\frac{\delta}{a}\right)^2 - \frac{2}{3}\left(\frac{\delta l_1}{a^2}\right) \tag{18}$$

where δl_1 is the distance from the middle of one arm to the point where the load is applied. The correction to the delamination crack length Δ is obtained through the experimental results by linear regression of the relation $C^{1/3}$ = f(a) (Figure 11). C is the compliance given by $C=\delta/P$.

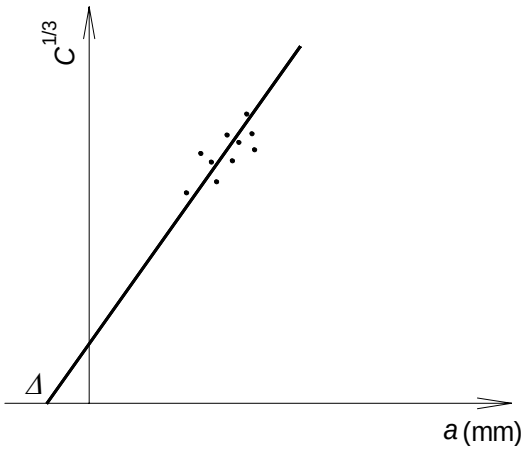

Figure 11 – Linear fit used to determine the correction Δ.

Modified compliance calibration (MCC)

This method is also proposed in [30] and establishes the relationship between the delamination crack length and the compliance by plotting the width normalized cube root of compliance $(BC)^{1/3}$ as function of the thickness normalized delamination length (a/2h) for the data of reloading. The slope of this regression is defined as m.

The critical energy release rate in mode I for delamination is given by:

$$G_{\mathrm{Id}} = \frac{3m}{2(2h)}\left(\frac{P}{B}\right)^2 \left(BC\right)^{2/3} F \tag{19}.$$

Compliance calibration method (CCM)

This method is proposed in [33]. Though the experimental points of C=f(a) a third degree polynomial is determined:

$$C = c_3 a^3 + c_2 a^2 + c_1 a + c_0 \tag{20}$$

The derivative of C in order to a is:

$$\frac{dC}{da} = 3c_3 a^2 + 2c_2 a + c_1 \tag{21}$$

Inserting (21) in the equation $G = \frac{P^2}{2B}\left(\frac{dC}{da}\right)$ then:

$$G_{Ic} = \frac{P^2}{2B}\left(3c_3 a^2 + 2c_2 a + c_1\right) \tag{22}$$

3.2.2. Comparison between curved and linear beam theories

The methodologies of calculation of G_{Id} presented in Section 3.2.1 are based on thin linear beam theory. However, it must be emphasised that the values of the compliance C are, in this case, obtained from specimens that are curved which can eventually affect the behaviour of the $P-\delta$ curves.

In this section a comparative study between thin linear beams and thin curved beams is presented by computing the differences in the values of the deflections provided by the two theories for different values of a. This study will give an estimation of the influence of the curvature on the values of G_{Id} calculated in curved specimens using formulas based on thin linear beam theory.

The formulas used are present in Roark's [34]. For thin linear beam theory:

$$\delta = \frac{Pa^3}{3EI} \tag{23}$$

where δ is the deflection produced by the load P, a is the length of the beam (in this case is the delamination length), E is the Young's modulus of the material and I is the second moment of area of the beam section.

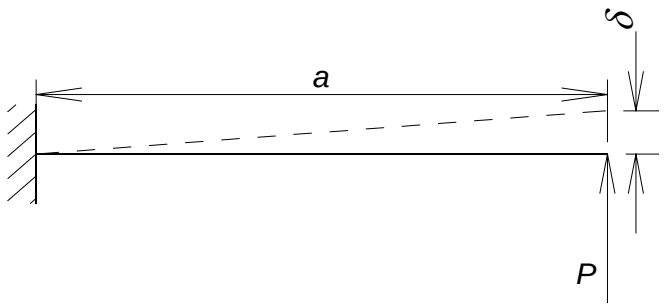

Figure 12 – Thin linear beam.

The cross section of the beam is shown in Figure 10 where B=21.7mm and h_1=6mm.

For thin curved beam:

$$\delta = \frac{R^3}{EI} L_{FV} \tag{24}$$

where

$$L_{FV} = P\left(\left(\theta+\phi\right)\sin\left(\theta\right)\sin\left(\phi\right) + \frac{1-\alpha+\beta}{2}\left(\theta+\phi+\sin\left(\theta\right)\cos\left(\theta\right)+\sin\left(\phi\right)\cos\left(\phi\right)\right) - \left(1-\alpha\right)\left(2\sin\left(\theta\right)\cos\left(\theta\right)-\sin\left(\theta\right)\cos\left(\phi\right)+\cos\left(\theta\right)\sin\left(\phi\right)\right)\right)$$

$$\beta = \frac{2F\left(1+\upsilon\right)\left(\frac{I}{RA}\right)}{R} \tag{25}$$

$$\alpha = \frac{I}{AR}$$

being R the radius to the centroid of the cross section, θ the one half of the total subtended angle of the arch, φ the angle measured counter clockwise from the midspan of the arch to the position of the concentrated load, A the area of the cross section, υ the Poisson's ratio and F is a shape factor of the cross section equal to $6/5$.

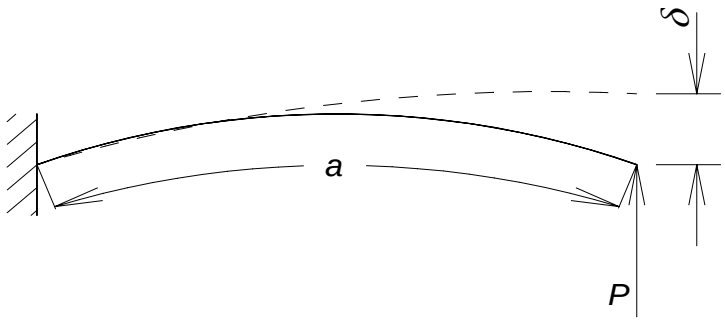

Figure 13 – Thin curved beam.

Figure 14 shows the evolution of the compliance in function of crack length *a* obtained from the two theories. The error obtained in the compliance between the two theories is presented in Figure 15.

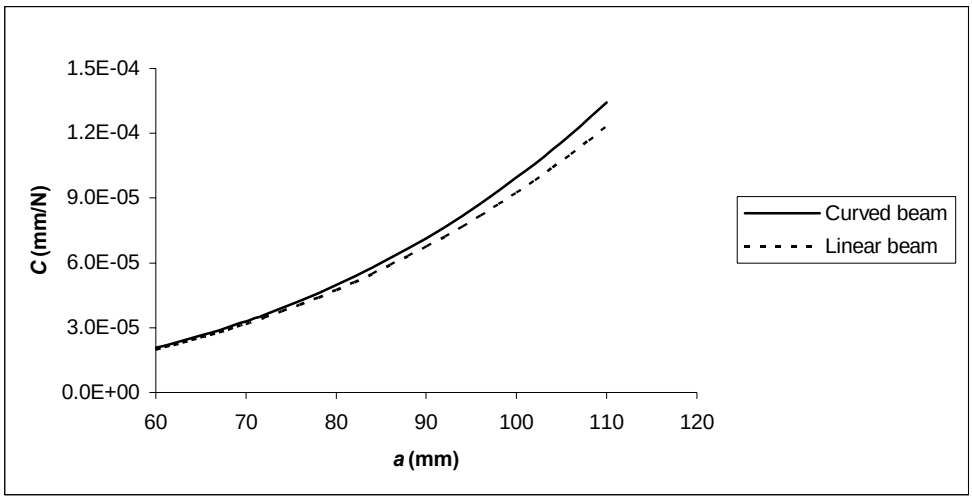

Figure 14 – Values of compliance provided by the two theories.

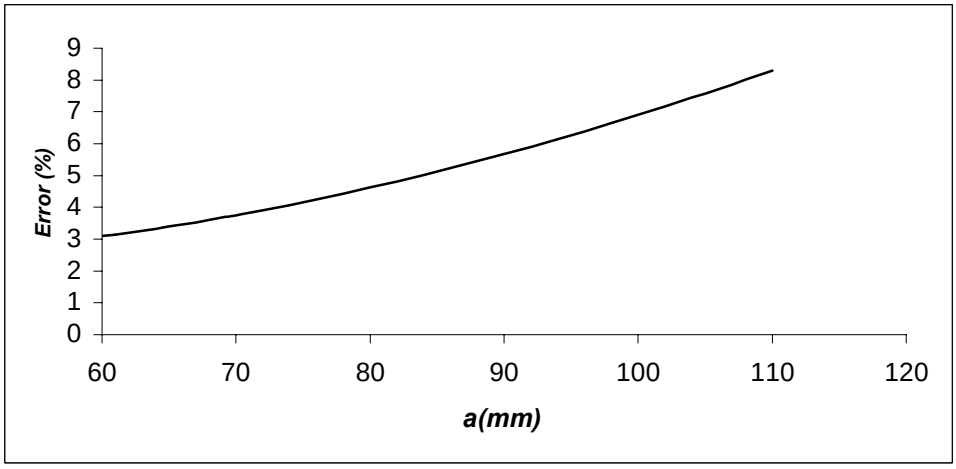

Figure 15 – Error evolution with crack length.

In Figures 14 and 15 is shown that the values of the compliance provided by the two theories are in reasonable agreement. For this particular case, the classical linear beam theory presented a deviation lower than 4% for the crack length range of interest. Therefore in this work it was considered quite reasonable to use the same formulas as for the DCB tests presented on Section 3.2.1, which are based on the classical linear beam theory.

3.3. Experiments

3.3.1. Specimens

Thirty specimens were cut-out from the referred GRP pipes. The pipes had the dimensions depicted in Figure 1. The composition of the pipes is described on Section 2.2. The mechanical properties of the pipes supplied by the manufacturer are given in Table I.

The opening of the precrack offered many difficulties due to the curved geometry of the specimens and due to the sand present in the pipes. The precrack, i.e. the initial 40mm, was opened with a power saw. Afterwards a manual saw was used to open the last 21mm so that the thickness of the precrack in its tip was as smallest as possible.

The average dimensions of the specimens are given in Table VI.

Table VI – Specimens dimensions.

L (mm)	B (mm)	h (mm)	a_0 (mm)
135	21.7	12	61

For load application two small L metallic beams (22x22 mm) were attached, using a commercial epoxy adhesive in the superior and inferior extremities of the specimens. The lateral surfaces of the specimens were painted with white ink and marked with vertical lines at 1mm interval, in order to easily measure the crack length. The specimens are depicted in Figure 16.

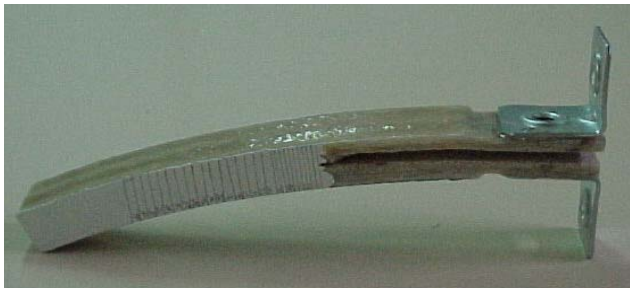

Figure 16 – Specimen.

Ten specimens were tested on the unconditioned state. Ten specimens were conditioned before tests take place in water at room temperature until they reached saturation in the conditioning chamber depicted in Figure 2a. Ten specimens were conditioned before tests take place in water at 50ºC until they reached saturation in the conditioning chamber depicted in Figure 2b. All the specimens were periodically removed from the conditioning chambers and after being carefully wiped out their weight was controlled in a digital scale in order to control the moment when saturation was reached.

3.3.2. Tests

The experimental tests were performed in a universal mechanical testing machine INSTRON according to the apparatus shown in Figure 17.

Figure 17 – Testing a sample.

The specimens were loaded at a cross head rate of 2mm/min. When delamination propagated 3mm the loading was stopped and the specimens were unloaded at a constant cross head rate of 25mm/min. After unloading, the

specimens were reloaded at a constant cross head rate of 2mm/min until delamination reached 45mm. The loading process was performed according to [30].

The $P-\delta$ curves were acquired continuously and the delamination length was controlled using a magnifying glass (3x).

3.3.3. Results

The values of G_{Id} considered at initiation and the corresponding *R-curves* were obtained from the $P-\delta-a$ values for the 28 considered valid specimens using the methods referred on Section 3.2.1.

The initiation values of G_{Id} for the unconditioned and preconditioned specimens are given in Table VII.

Table VII – Initiation values of G_{Id} (N/mm) for the unconditioned and preconditioned specimens.

Initiation values of G_{Id} (N/mm)									
Specimen	**Unconditioned**			**Water at room temperature**			**Water at 50ºC**		
	CBT	MCC	CCM	CBT	MCC	CCM	CBT	MCC	CCM
1	0.3302	0.3301	0.1095	0.2268	0.2304	0.3319	0.3464	0.3609	0.2835
2	0.6088	0.6372	0.8776	0.2544	0.2505	0.1346	0.1634	0.16945	0.2270
3	0.5413	0.5607	1.0922	0.2541	0.2539	0.3242	0.1865	0.1854	0.1375
4	0.2824	0.2971	0.5215	0.1689	0.1716	0.2114	0.2807	0.2758	0.1889
5	0.4145	0.4141	0.7284	0.4634	0.4584	0.1651	0.3210	0.3609	0.2045
6	0.4422	0.4586	0.3037	0.1098	0.1078	0.0494	0.2139	0.2107	0.1026
7	0.6727	0.6591	1.0592	0.2047	0.2097	0.2233	0.2619	0.2677	0.5326
8	0.2949	0.2967	0.5335	0.1961	0.1973	0.2955	0.2504	0.2524	0.4802
9	0.4790	0.4779	0.2544	0.1936	0.1920	0.1364	0.3072	0.3106	0.4120
10	0.5149	0.5111	0.4048	-	-	-	-	-	-
Average	**0.4581**	**0.4643**	**0.5885**	**0.2302**	**0.2302**	**0.2080**	**0.2591**	**0.2660**	**0.2854**
St. dev.	**0.131**	**0.132**	**0.340**	**0.098**	**0.096**	**0.096**	**0.062**	**0.0699**	**0.1540**

Some of the obtained *R-curves* are depicted in Figures 18-20.

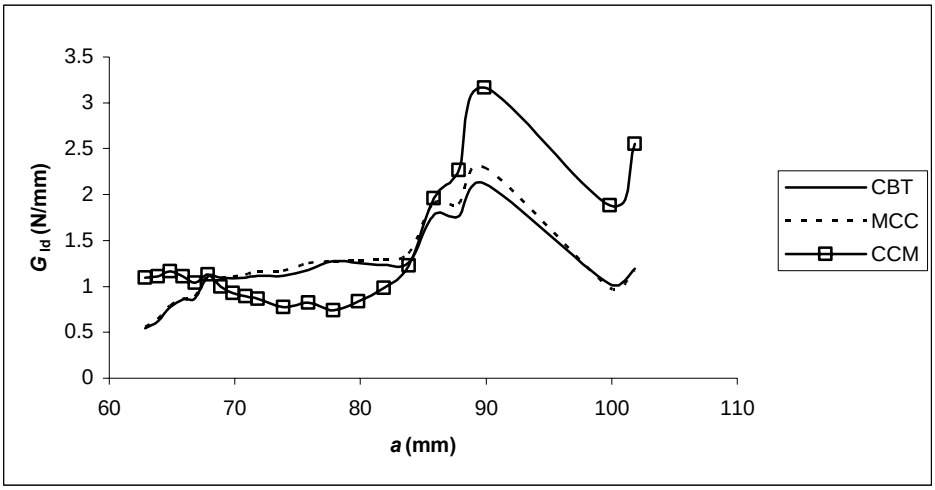

Figure 18 – *R-Curves* of an unconditioned specimen.

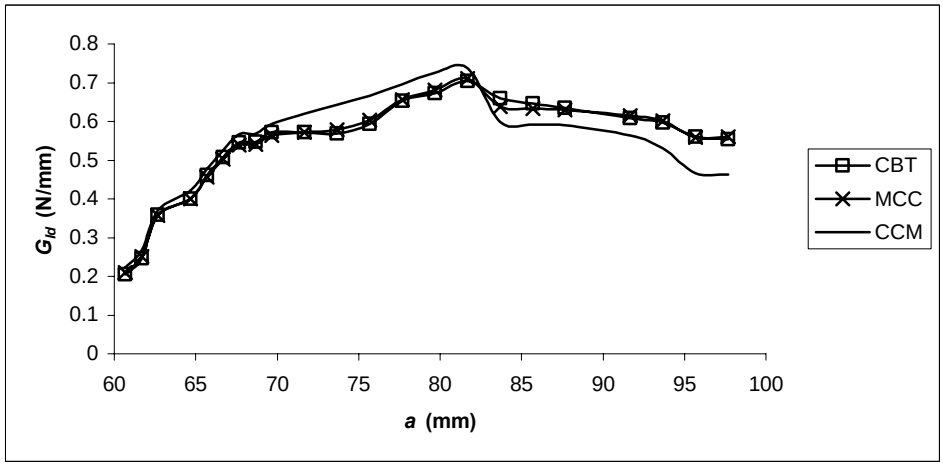

Figure 19 – *R-curves* of a specimen saturated in water at room temperature.

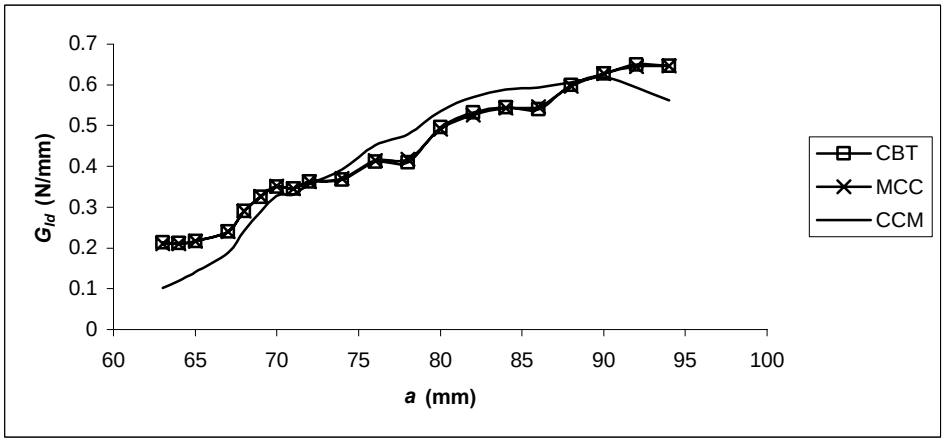

Figure 20 – *R-Curves* of a specimen saturated in water at 50ºC.

In typical resistance curves the values of G_R are approximately constant with increasing crack length [30]. In the present case atypical resistance curves were obtained as depicted in Figures 18-20. The values of G_R shows pronounced variations with increasing crack length. This is mainly due to the fibre bridging effects and unstable crack propagation which occur during delamination progression. Because of these phenomena it was considered that G_{Id}=G_R at initiation.

Corrected beam theory and method of compliance calibration gave similar values for G_{Id}. With these techniques a high scatter was measured. This can be related, mainly, with the fibre bridging effects and with the complex heterogeneous composition of these pipes. Therefore, for G_{Id} calculation were only taken into account the values closer to the average value, represented in Table VIII.

Table VIII - G_{Id} values closer to the average value.

Initiation values of G_{Id} (N/mm)						
Specimens	**Unconditioned**		**Water at room temperature**		**Water at 50ºC**	
	CBT	MCC	CBT	MCC	CBT	MCC
1	0.5413	0.5607	0.2268	0.2304	0.281	0.276
2	0.4145	0.4141	0.2544	0.2505	0.214	0.211
3	0.4422	0.4586	0.2541	0.2539	0.262	0.268
4	0.4790	0.4779	0.2047	0.2097	0.250	0.252
5	0.5149	0.5111	0.1961	0.1973	0.307	0.311
6	-	-	0.1936	0.1920	-	-
Average	**0.4784**	**0.4845**	**0.2216**	**0.2223**	**0.263**	**0.263**
St. dev.	**0.0517**	**0.0552**	**0.0279**	**0.0267**	**0.035**	**0.036**

The compliance calibration method (CCM) showed a high scatter of the measured G_{Id}. This is easily explained observing the C=f(a) curves, i.e. their evolution is almost random disagreeing with the theoretical expectation. As the compliance calibration method uses the values of the polynomial regression

based on the curve C=f(a) (which doesn't present the expected evolution) this method fails when calculating the G_{Id} values.

3.4. Numerical analysis

The specimens curvature can have significant influence on this type of test, i.e. the mode I loading can lead to a mixed mode situation (mode I plus mode II). Therefore the influence of mode II on the calculated G_{Id} values may prevail. For the present case the influence of the geometry on the values of G_{Id} was quantified using the finite element method. Interface elements previously developed [31-32] were programmed into ABAQUS® software to simulate the initiation and propagation of the crack.

3.4.1. Cohesive mixed-mode damage model

Crack growth was simulated using the interface elements presented in [31-32, 35]. The zero thickness 6-node interface elements (Figure 21) are compatible with the 8-node two-dimensional continuum elements (CPE8R) of ABAQUS® software.

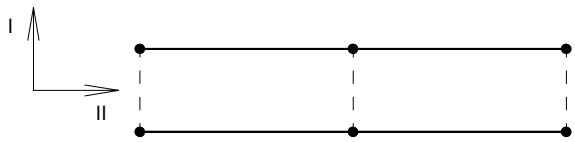

Figure 21 – The interface element

The interface element formulation is based on constitutive interface stress/relative displacement relations for the damaged and non-damaged states [32]. In the non-damaged state interfacial stresses are obtained from:

$$\boldsymbol{\sigma} = \mathbf{D}\boldsymbol{\delta}\,, \tag{26}$$

where **D** is a diagonal matrix including the initial interface stiffness. After the local cohesive limiting stress is attained, there is a linear softening relationship between stresses and relative displacements simulating a cohesive fracture

process zone at the crack tip [32]. In pure modes, the area bounded by the stress-relative displacement relationship is equated to the respective critical strain energy release rate:

$$G_{\mathrm{ic}} = \frac{1}{2}\sigma_{u,i}\delta_{u,i} \tag{27}.$$

Using the measured G_{Ic} and local cohesive strength values, the relative displacement for which complete failure occurs $\delta_{u,i}$ (i=1, 2), can be determined [32].

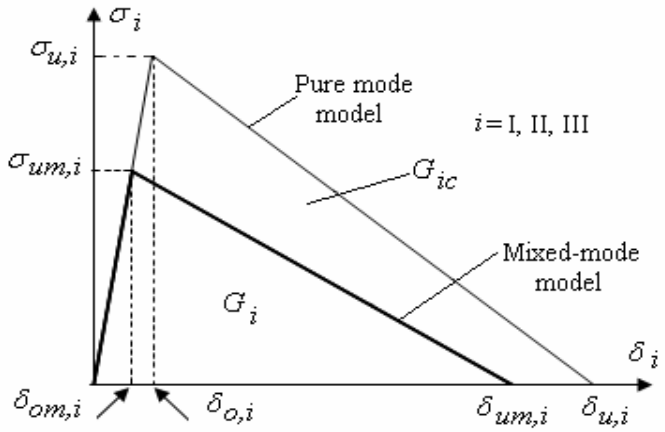

Figure 22 – The linear softening law for pure mode and mixed mode

The constitutive equation for the softening stress/relative displacement relationship simulating gradual material degradation is:

$$\boldsymbol{\sigma} = \left(\mathbf{I} - \mathbf{E}\right)\mathbf{D}\mathbf{d} \tag{28}$$

where **I** is the identity matrix, **E** a diagonal matrix containing the damage parameters:

$$e_i = \frac{\delta_{u,i}\left(\delta_i - \delta_{o,i}\right)}{\delta_i\left(\delta_{u,i} - \delta_{o,i}\right)} \tag{29}.$$

For mixed mode loading a quadratic stress based criterion is used to simulate damage initiation. Assuming that normal compressive stress does not induce damage [32] it can be written:

$$\left(\frac{\sigma_{\mathrm{I}}}{\sigma_{u,\mathrm{I}}}\right)^2+\left(\frac{\sigma_{\mathrm{II}}}{\sigma_{u,\mathrm{II}}}\right)^2=1 \quad \text{if} \quad \sigma_{\mathrm{I}}\geq 0$$
$$\sigma_{\mathrm{II}}=\sigma_{u,\mathrm{II}} \quad \text{if} \quad \sigma_{\mathrm{I}}\leq 0 \tag{30}.$$

Damage propagation is simulated considering a linear energetic criterion:

$$\frac{G_I}{G_{Ic}}+\frac{G_{II}}{G_{IIc}}=1 \tag{31}$$

where the energy release in each mode at complete failure is obtained from the area of the minor triangle of Figure 22:

$$G_i=\frac{1}{2}\sigma_{um,i}\delta_{um,i} \tag{32}$$

where $\sigma_{um,i}$ is the local cohesive stress in each mode leading to damage initiation, and $\delta_{um,i}$ the critical relative displacement in each direction for which complete failure occurs (see Figure 22). Considering mixed mode ratio parameters $\beta_i=\delta_i/\delta_I$, an equivalent mixed mode relative displacement $\delta_e=\sqrt{\delta_{\mathrm{I}}^2+\delta_{\mathrm{II}}^2}$ and equations (26), (27), (30), (31) and (32), the relative displacement at damage initiation ($\delta_{om,i}$) and at complete failure ($\delta_{um,i}$) in each mode can be written as:

$$\delta_{om,i}=\frac{\beta_i\delta_{om}}{\sqrt{1+\beta_{\mathrm{II}}^2}} \tag{33}$$

$$\delta_{um,i}=\frac{\beta_i\delta_{um}}{\sqrt{1+\beta_{\mathrm{II}}^2}} \tag{34}$$

where δ_{om} and δ_{um} are the onset and ultimate equivalent mixed-mode relative displacements. The damage parameter can now be obtained substituting equations (33) and (34) in equation (29).

3.4.2. Model description

The DCB tests of specimens cut-out from GRP pipes in the circumferential direction was represented by a FEM mesh with 26112 quadratic elements (8-node 2D continuum elements CPE8R) and 150 interface compatible elements disposed along the mid-plane of the uncracked region, as depicted in Figures 23-24.

The specimens geometry considered is represented in Figure 10. The specimens dimensions are the average dimensions of the tested specimens shown in Table VI.

The material properties considered in the numerical simulation are listed in Table IX.

Table IX – Mechanical properties of the GRP pipes

E_c MPa	$E_r = E_L$ MPa	$\nu_{cr} = \nu_{cL}$	ν_{rL}	σ_{um} MPa	$G_{cr} = G_{cL}$ MPa	G_{rL} MPa	G_{Id} N/mm	G_{IId} N/mm
10547	3808	0.3	0.4	20	1000	800	0.47	1.2

As explained in [32], the critical energy release rates are input data in the damage model. The input value of G_{Id} is the value obtained in the previous experiments for the unconditioned specimens. The $P-\delta-a$ values obtained numerically considering mixed-mode (I and II) damage propagation, were used to achieve a new value of G_{Id} which was compared with the experimental value (input) [32]. The difference between the numerical values of G_{Id} and the experimental (input) ones gave an idea of the influence of mode II in the values of G_{Id}.

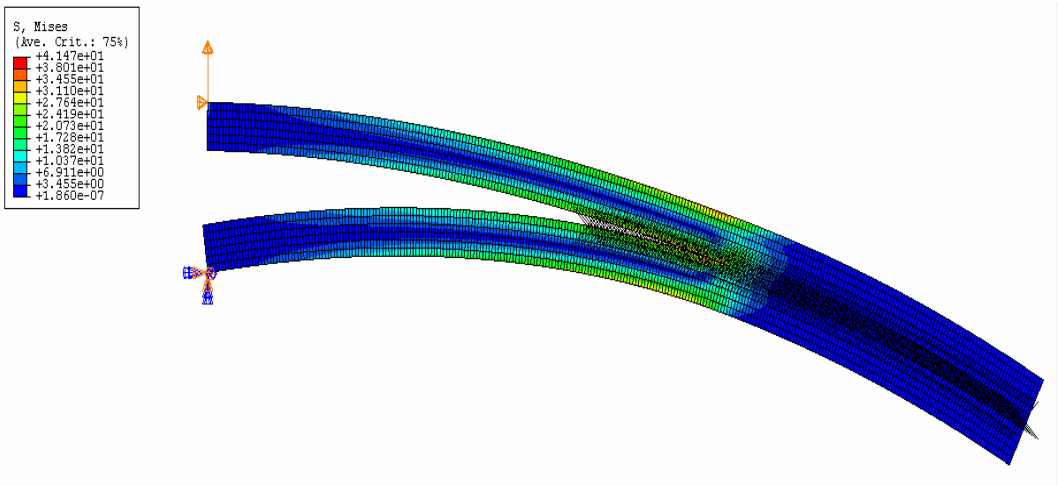

Figure 23 – Finite element mesh.

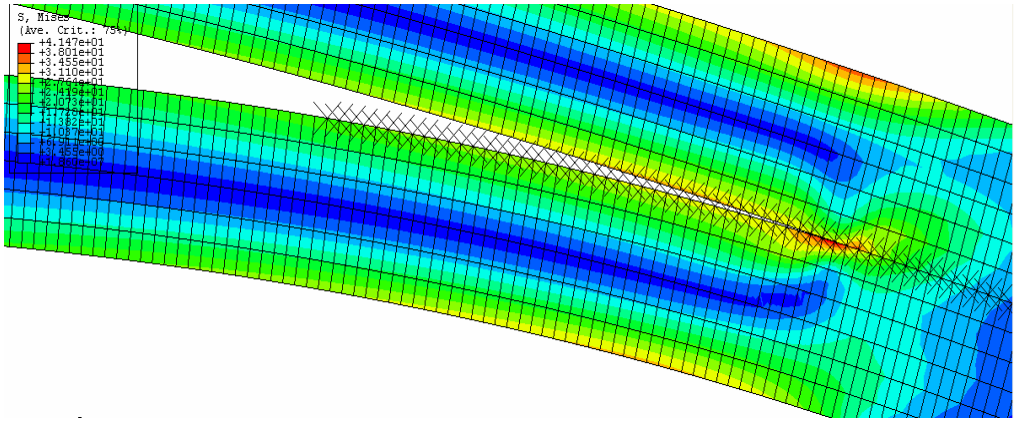

Figure 24 – Detail of the crack zone. Interface elements are represented by diagonal crosses.

The boundary conditions reproduce the experimental ones, so, the lower left corner of the specimen was fixed and the movement of the upper left corner was restricted in the circumferential direction as depicted in Figure 23. A loading displacement (δ_{max}=30mm) was applied incrementally at the upper left corner of the specimen (Figure 23), considering a very small increment value (0.2%) to ensure a smooth propagation process.

3.4.3. Numerical results

The $P-\delta$ and *P-a* curves obtained from the numerical model are represented in Figures 25-26.

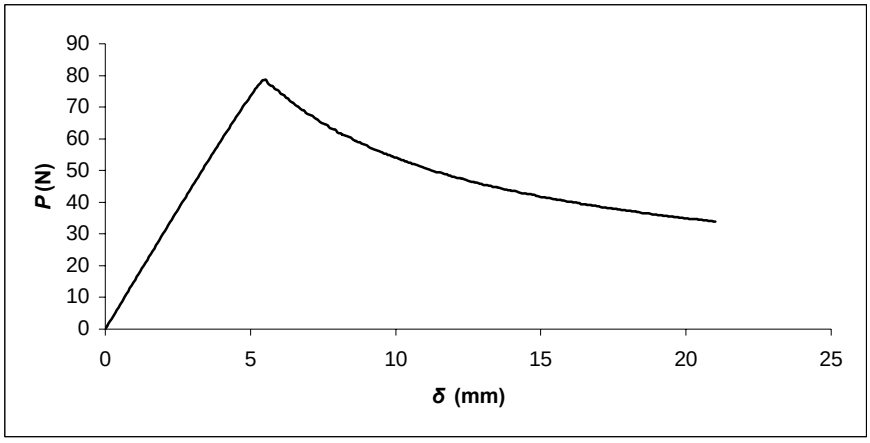

Figure 25 – $P-\delta$ curve obtained from the FEM model.

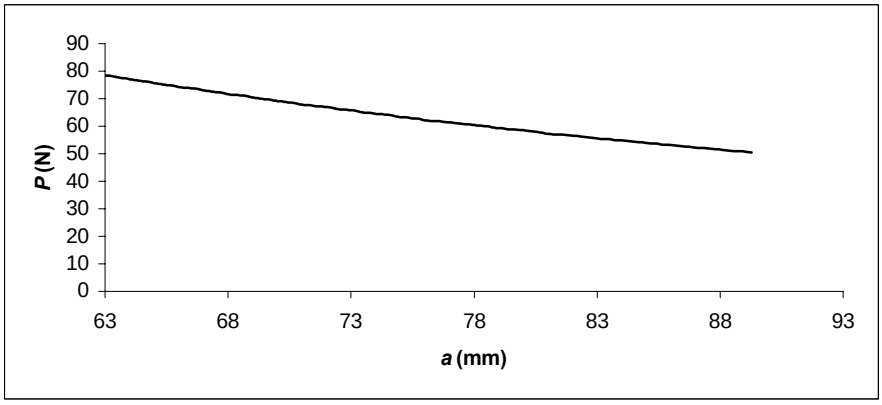

Figure 26 – *P-a* curve obtained from the FEM model.

Once the maximum force is attained, a stable crack propagation accompanied by a decrease in the force can be observed.

Starting from the obtained values of force (P), displacement (δ) and crack length (a) the critical strain energy release rate was determined using the three different calibration methods described in Section 3.2.1. After obtaining the G_{Id} values given in Table X, the *R-curves* were plotted as depicted in Figure 27.

Table X – Numerical results

Theory	G_{Id} (N/mm)
CBT	0.4692
MCC	0.5035
CCM	0.4751

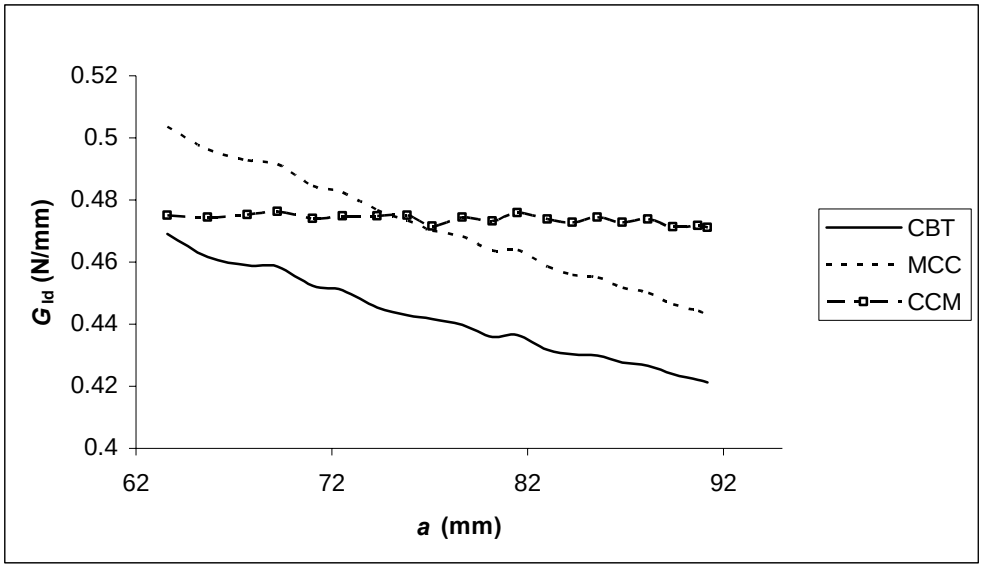

Figure 27 – Numerical R-curves.

Table XI – Comparison of results

Theory	G_{Id} reference (N/mm)	G_{Id} numerical (N/mm)	Error (%)
CBT	0.470	0.4692	0.2
MCC	0.470	0.5035	7.1
CCM	0.470	0.4751	1.1

From these results it was concluded that the deviations produced by the mode II in the initiation values of G_{Id} are not very significant. The maximum error obtained is 7% using modified compliance calibration. The corrected beam theory provided the best result with a negligible error.

3.5. Conclusions

It was seen that moisture has a pronounced effect on the values of the critical strain energy release rate (G_{Id}) of GRP pipes and that the influence of the temperature of the preconditioning on the G_{Id} values is negligible. The G_{Id} value determined for the unconditioned specimens was 0.47 N/mm and for the conditioned specimens was 0.22 N/mm. These values were obtained using corrected beam theory and modified compliance calibration. Compliance calibration method

is not appropriate to use in these kind of tests due to the phenomena that occur during the tests (unstable crack growth and fibre bridging) which affects the quality of the polynomial regression based on the C=f(a) curve used in this calibration method.

A numerical simulation was performed to evaluate the influence of spurious mode II loading introduced by the specimen's geometry using ABAQUS® 2D elements with interface finite elements specially developed. The numerical simulation showed that the mode II effect in the tests is negligible (0.2%) when the G_{Id} values are obtained using corrected beam theory. Therefore it was proved that DCB standard procedures are applicable for the present case.

4. Influence of moisture absorption on creep of GRP pipes

4.1. Introduction

High-performance polymer composites exhibit a time-dependent degradation in modulus (creep or stress relaxation) and strength (creep rupture) as a consequence of the viscoelasticity of the polymer matrix [19, 36]. One of the most important aspects of long-term durability and dimensional stability of these materials is their long-term creep behaviour. Prediction of long-term integrity of any polymeric composite structure depends on the viscoelastic properties of these materials [19, 36-37]. However, long-term properties prediction of GRP pipes remains a difficult task because extensive mechanical tests on the components are required [38].

The most common accelerated test method currently used applies the so called Time-Temperature Superposition Principle (TTSP). This principle allows the extrapolation based on short-term tests at different temperatures [5, 19, 36-42]. Many researchers used the TTSP in order to predict the long-term properties of polymeric materials and fibre reinforced polymer composite materials.

Julius [36] made short-time three-point bending creep tests on commercial polymers in a Dynamic-Mechanical-Thermal Analyser (DMTA) using different temperatures and applied the TTSP to the experimental data to obtain the master curve for predicting the long-term creep compliance. The master curve was then compared with the results of long-term bending experiments. It was shown that the long-term creep compliance can be well predicted using the TTSP for some kinds of specimens. For other specimens the predictions of creep compliance obtained using TTSP showed pronounced deviations from the experimental results.

Yao [38] performed short and long-term creep tests on specimens cut-out from GRP pipes in order to predict their long-term properties. Due to the difficulties on applying the TTSP on GRP pipes, Yao [38] established the equivalence between moisture and temperature by proposing a moisture-aging superposition principle and applied it on results of three-point bending tests on small samples to predict long-term properties from short-term data.

Feng [40] tested wet and dry epoxy adhesives on a DMTA machine in torsional mode at several temperatures and frequencies. He applied the TTSP to the experimental results and obtained a master curve, allowing for the long-term creep compliance to be estimated. The temperature and moisture effects were also investigated by means of mechanical responses and were found to have equivalent effects on mechanical response. The TTSP is suitable for constructing a long-term creep master curve of these investigated epoxy adhesives. The creep behaviour of the studied materials can be reliably predicted using a set of short-term accelerated creep tests.

Goertzen [42] studied the creep behaviour of carbon fibre/epoxy matrix composites through tensile and flexural creep testing. Tensile creep tests were performed and a power law relation was fitted to the experimental creep curves allowing the prediction of the tensile compliance values at the end of the design life of the material (50 years). Flexural creep tests were performed using a DMTA machine. The TTSP was applied to the experimental results allowing the prediction of the flexural compliance and the modulus reduction at the design life of the material. According to the 50 year predictions (made using the tensile creep data and using a maximum strain failure criterion) the material does not fail when loaded with 77% of the ultimate tensile strength. These values are in assumption with the results obtained using the TTSP which predict that the stress level required to promote failure at the 50 year point (at a constant temperature of 30ºC) would be approximately 84% of the ultimate tensile strength. The results of the flexural creep tests also show that the 50 year failure stress decreases while reference temperature increases and that the values of the 50 year reduction in flexural modulus increases while the reference temperature increases.

Miyano [43] predicted the long-term flexural fatigue life of plain woven carbon fibre/vinylester (CFRP) laminates and plain woven glass fibre/vinylester (GFRP) laminates using a methodology based on the TTSP. It was concluded that the flexural fatigue strengths for the CFRP and GFRP decreases strongly with increasing time and temperature. The flexural fatigue strength of CFRP laminates decreases scarcely with increasing number of cycles to failure while that of GFRP laminates decreases strongly with increasing number of cycles to failure.

One of the most important factors which affect the creep behaviour of fibre reinforced plastic materials is moisture. Water penetrates the resin and attacks the matrix, the reinforcement and the interface of several composite materials [44]. Some of the hygrothermal aging effects are reversible like the effect on T_g (reversible when the

material dries) and others are not, like the plasticization of the matrix and post-cure reactions [5].

In this section creep and DMTA tests were performed in unconditioned and preconditioned specimens machined from GRP pipes in order to measure and predict the influence of moisture on its long-term behaviour. On the DMTA tests the specimens were subjected to flexure and the storage modulus (*E'*) and the loss tangent (tan δ) were measured. The TTSP and a power law extrapolation method were applied to the experimental data to predict the long-term modulus of the material.

The predictions of long-term modulus obtained using TTSP and the power extrapolation method were compared with the real-time creep data. The creep tests were performed on GRP pipes subjected to two different preconditioning environments [1]. The obtained creep data was treated in order to determine the variation of the circumferential modulus occurred during the tests. Although the creep tests aren't similar to the DMTA tests, the comparison of the results of the two experimental tests gave an idea of the ability of the TTSP and the Power Law extrapolation method to predict the long-term circumferential modulus of the analysed pipes. The comparisons of the DMTA test results of specimens conditioned in different environments enabled the assess to the hygrothermal effects on the instantaneous modulus and viscoelasticity of the material.

4.2. Materials and specimens

The specimens for the creep tests are depicted in Figure 28 and its mechanical properties are described on Table I.

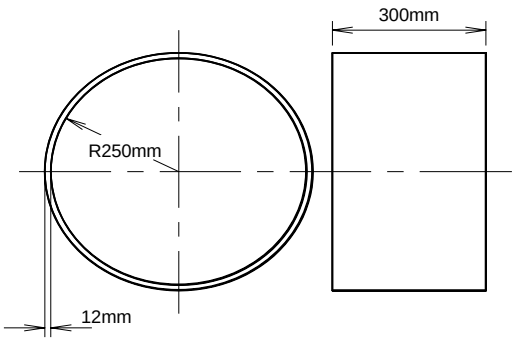

Figure 28 – Creep specimens.

The DMTA test coupons were machined from the pipes using a power saw. Since DMTA test setup requests small thickness two types of specimens were used. One was machined from a region closer to the inside layer of the specimen (Type 1) and other one was cut-out from a region closer to the outside layer (Type 2) as it is shown in Figure 29.

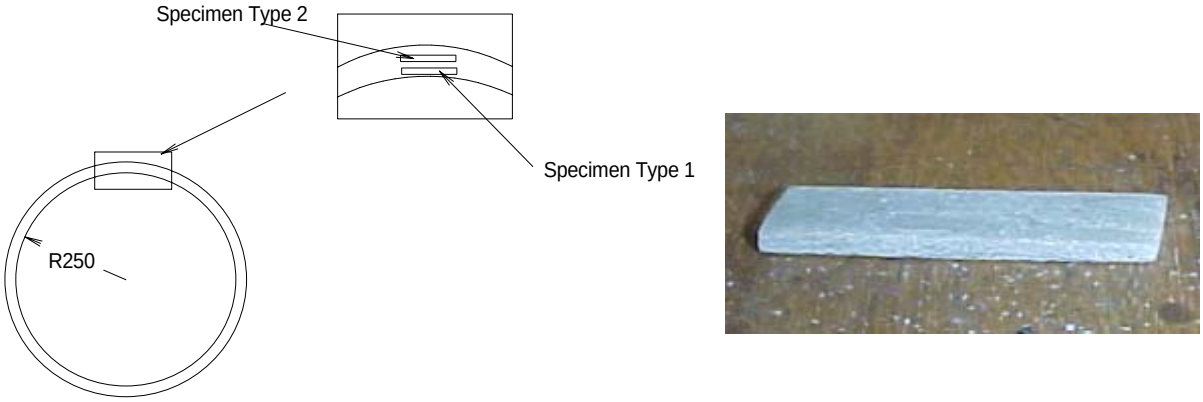

Figure 29 – DMTA specimens.

The average dimensions of the DMTA specimens are depicted on Table XII.

Table XII – Average dimensions of the DMA specimens.

	Length (mm)	**Width (mm)**	**Thickness (mm)**
Average dimensions	41.42	10.47	3.22

The length corresponds to the circumferential direction of the pipe and the width corresponds to the longitudinal direction of the pipe. Fifteen specimens of each type were machined using a power saw.

Burn-off tests were performed according to the standard procedure NP 2216 1988 on 5 specimens type 1 and 5 specimens type 2 removed from the pipes in order to analyse the components and the structure of the specimens as depicted in Figure 30.

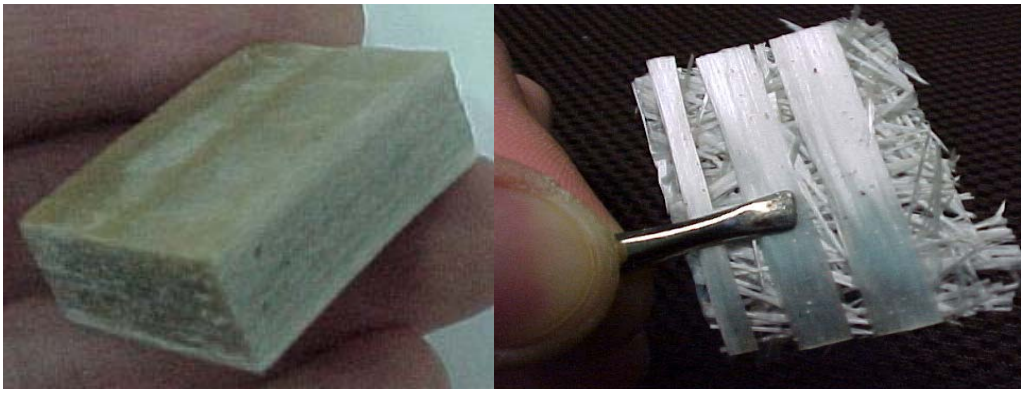

(a) (b)

Figure 30 – (a) Sample for burn-off test; (b) Fibre reinforcement obtained after burn-off.

The structure of the pipes is heterogeneous and it is constituted by roving, random matt, polyester resin and sand according to the values depicted on Table XIII.

Table XIII – Relative composition of GRP pipes for mass content (%).

Constituents	Average values	Standard deviation
Polyester (matrix)	35.65	0.41
Fibre (Matt + Roving)	23.47	0.41
Roving	10.41	1.51
Matt	12.66	0.88
Sand	41.28	2.54

The composition of samples type 1 and 2 is depicted on Tables XIV and XV.

Table XIV – Relative composition of type 1 samples for mass content (%).

Constituents	Average values	Standard deviation
Polyester (matrix)	34.82	2.05
Fibre (Matt + Roving)	35.15	2.05
Roving	14.58	1.84
Matt	20.57	2.87
Sand	30.04	5.90

Table XV – Relative composition of type 2 samples for mass content (%).

Constituents	Average values	Standard deviation
Polyester (matrix)	31.35	1.77
Fibre (Roving + matt)	20.03	1.77
Roving	9.24	1.31
Matt	10.79	1.51
Sand	48.63	2.53

The differences detected between inner layers and outer layers of the pipes are explained by the heterogeneity of the pipes structure.

4.3. Tests

4.3.1. Creep tests

The creep tests were carried out following the European standard EN 1227:1997 [45] used to determine the long-term ultimate relative ring deflection under wet conditions on glass-reinforced thermosetting plastics (GRP) pipes.

Creep tests were performed in GRP pipes in order to measure its creep compliance during the experimental tests. Most of these tests were performed and described by Faria [1].

Experimental creep tests were performed applying a constant load to the specimen submerged in water at room temperature and its deflection was measured periodically. The loading scheme is depicted in Figure 31.

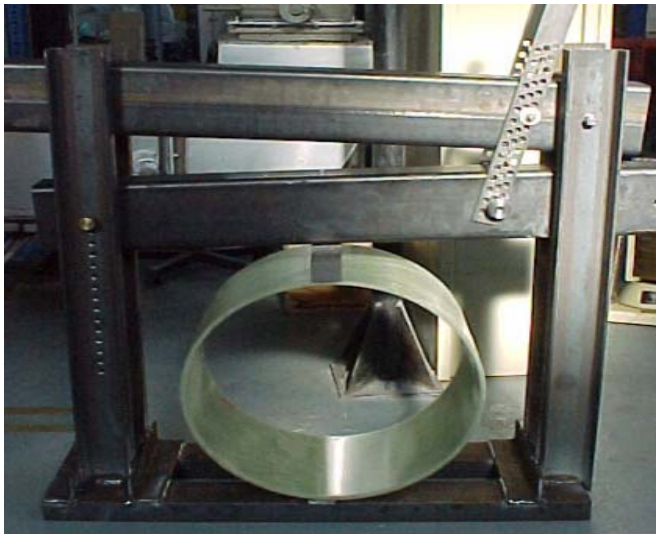

Figure 31 – Creep test apparatus [1].

Faria [1] performed creep tests on 18 unconditioned specimens using several load levels (10 to 14 kN). The creep tests were performed with the specimens submerged in water at room temperature. Creep tests were also performed on specimens preconditioned in water at 50ºC [1]. After preconditioning the specimens were tested in creep submerged in water at room temperature. In Table XVI are listed all the tested specimens, indicating the applied creep load and preconditioning.

Table XVI – Creep specimens with the correspondent load and preconditioning.

Specimen nº	Preconditioning	Load (kN)
C36	No	12.196
C46	No	11.831
C47	No	12.087
C55	No	12.400
C56	No	12.400
C38	No	10.643
C50	No	10.380
C52	No	10.431
C39a	No	12.719
C48	No	12.830
C49	No	12.692
C51	No	13.638
C57	No	13.088
C39b	No	13.970
C45	No	14.420
C58	No	13.988
C53	No	11.411
C54	No	11.139
C88	50ºC during 4920 hours + 3000 hours at dry air	11.096
C89	50ºC during 4920 hours + 3000 hours at dry air	11.096
C92	50ºC during 4920 hours + 3000 hours at dry air	11.353
C90	50ºC during 7112 hours	9.865
C91	50ºC during 7112 hours	10.567
C93	50ºC during 10800 hours	9.084
C94	50ºC during 10800 hours	10.059
C95	50ºC during 10800 hours	11.358

4.3.2. DMTA tests

The experimental tests were performed on a DMTA machine of Polymer Laboratories® [46].

Fifteen specimens of each type were obtained. Specimens type 1 were cut-out from the inner part of the structure and specimens type 2 were cut-out from the outer part of the structure. Ten specimens (5 of each type) were tested in the DMTA without any conditioning. Other 10 specimens (5 of each type) were tested in the DMTA after being saturated in water at room temperature. The last 10 specimens (5 of each type) were tested in the DMTA machine after being saturated in water at 50ºC.

The DMTA machine has a unit for flexural loading of composite materials with displacement control. The machine is also equipped with an oven to impose the thermal environment (constant, ramp or by step). The control of the test, the data acquisition and data processing were performed using the THERMAL V500 software [46]. This software was also used on the calibration of the measure system according to the manufacturer procedure.

The specimens were fixed on the machine as cantilever beams (Figures 32-33). The torque applied to the fixing screws was 30cN.m. The specimens were tested at different temperatures, from 25ºC to 160ºC by steps of 5ºC. At each test temperature a frequency scan was performed for several frequencies (0.01, 0.1, 0.2, 0.3, 1, 2, 3, 5, 10, 20, 30, 50 and 100 Hz). The amplitude of the harmonic displacement applied to the specimens was 8μm as depicted in Figure 32.

Figure 32 – Cantilever beam set-up used for DMTA tests.

Figure 33 – DMTA tester.

4.4. Data reduction schemes

Three data reduction schemes were used to process creep and DMTA experimental data. In creep tests the applied load was constant and the deflection of the specimens was periodically controlled. The experimental data was reduced to the time evolution of the circumferential modulus. The DMTA data, storage modulus and loss *tan*, were converted into relaxation modulus [47]. Time-Temperature Superposition Principle with 25ºC as the reference temperature and an extrapolation using a power law relation applied to the DMTA data obtained at 25ºC were used to predict the long-term circumferential modulus.

4.4.1. Creep data reduction scheme

The circumferential elastic modulus E, function of the maximum deflection y, can be calculated using the formulas given on Roark's [34]:

$$E = -\frac{k}{y}W \tag{35}$$

where:

$$k = \frac{R_m^3}{I}\left(\frac{\pi\left(1-\frac{h}{R_m}+\frac{2F(1+\upsilon)h}{R_m}\right)}{4} - \frac{2\left(1-\frac{h}{R_m}\right)^2}{\pi} \right) \tag{36}$$

and:

$$h = c\left[\frac{R_m}{c} - \frac{2}{\ln\left(\frac{R_m/c+1}{R_m/c-1} \right)} \right] \tag{37}.$$

On Equations 35-37 W is the applied load, R_m is the average radius of the pipes, c is the thickness, I is the second moment of inertia of the cross section of the pipes and F is the shape factor of the cross section and is equal to 6/5. In the present case the circumferential elastic modulus is given by:

$$E = -57988.76\frac{W}{y} \tag{38}.$$

During the creep tests the load is prescribed as constant and the maximum deflection $y(t)$ becomes time dependent as well as the modulus $E(t)$ which can be obtained from the previous elastic solution assuming a linear viscoelastic behavior and applying the Elastic-Viscoelastic Correspondence Principle [48] as:

$$E(t) = -57988.76\frac{W}{y(t)} \tag{39}.$$

In fact this is not the real relaxation modulus but the reciprocal of creep compliance. The relaxation modulus can be obtained using the simple approach suggested by Park et al. [49]. However in this case the differences were negligible.

Finally the time-dependent circumferential modulus, calculated using Equation 39, was compared with the predictions made using DMTA test data.

4.4.2. DMTA data reduction scheme

When a viscoelastic material is subjected to a simple harmonic strain, with a w angular frequency, the resultant stress in permanent regime is also harmonic, with the same angular frequency but with a phase difference δ [5]. Considering the complex representations of stress and strain:

$$\varepsilon^* = \varepsilon_0 e^{iwt} \quad \text{and} \quad \sigma^* = \sigma_0 e^{i(wt+\delta)} \tag{40}.$$

The linear viscoelastic behaviour is defined by the complex modulus [5], given by:

$$E^* = \frac{\sigma^*}{\varepsilon^*} = E' + iE'' \tag{41}.$$

The real part of the complex modulus, *E*', is defined as storage modulus [5]:

$$E' = \frac{\sigma_0}{\varepsilon_0} cos(\delta) \tag{42}$$

and the imaginary part, *E''*, is defined as loss modulus [5]:

$$E'' = \frac{\sigma_0}{\varepsilon_0} sen(\delta) \tag{43}.$$

The ratio between the loss modulus and the storage modulus is the loss tangent (*tan* δ) [5]:

$$\tan(\delta) = \frac{E''}{E'} \tag{44}.$$

The DMTA machine measures the displacement applied to the specimen and the correspondent flexural force. By knowing the amplitudes of the force, F_0, and of the displacement, f_0, as well as the complex rigidity (*S'* and *S''*) and the vibrating mass *M* of the loading apparatus, the modulus *E'* and *E''* are obtained through [46]:

$$\begin{aligned} kE' &= \frac{F_0}{f_0}\cos(\delta) + Mw^2 - S' \\ kE'' &= \frac{F_0}{f_0} sen(\delta) - S'' \end{aligned} \tag{45}.$$

On Equation 45, k is a rigidity geometric factor, which for the geometry of the tested specimens has the value of 2.9, according to [46].

The used DMTA machine (Figure 33) makes calculations and illustrates the curves of the storage modulus and loss tangent for each temperature and frequency of loading.

Two data reduction schemes were applied to the DMTA results.

4.4.2.1. Time temperature superposition principle

Through DMTA tests is obtained the variation of the storage modulus and loss *tan* with temperature and frequency. For many polymers it is possible to shift the obtained curves at different temperatures to form a master curve, by superposition, for a reference temperature [5].

The TTSP uses the temperature as an acceleration factor of the mechanical response based in the idea that the short-term mechanical behaviour at higher temperatures is equivalent to the long-term mechanical behaviour at lower temperatures. According to TTSP a transitory property $P(T,t)$ (temperature T at the time t) is the same as the property $P(T_0, \psi)$ (reference temperature T and reduced time ψ) with:

$$P(T,t) = P(T_0,\Psi) \text{ e } \Psi = \frac{t}{a_\Gamma} \tag{46}$$

where a_Γ is the shift factor and is determined experimentally. By the same way the frequency-temperature principle establishes that the viscoelastic dynamic properties, P^*, satisfies the identity $P^*(T,w) = P^*(T_0,\Phi)$ where $\Phi = wa_\Gamma$ is the angular reduced frequency [5].

Through this technique (TTSP) a master curve of the viscoelastic properties of the material is obtained in a larger range of frequencies or time as depicted in Figures 34-35. The shift factor a_Γ is temperature dependent and is described by the Arrhenius law:

$$\log\left(a_{\Gamma}\right)=\frac{\Delta H}{2.303R}\left(\frac{1}{T}-\frac{1}{T_0}\right) \tag{47}$$

where ΔH is the activation energy, R is the universal constant of perfect gases, T is the temperature and T_0 is the reference temperature [36].

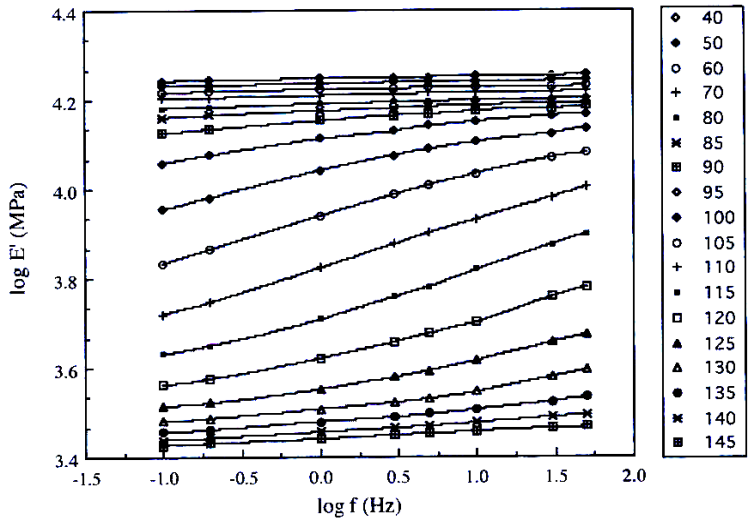

Figure 34 – Typical evolution of the storage modulus with varying temperatures and frequencies.

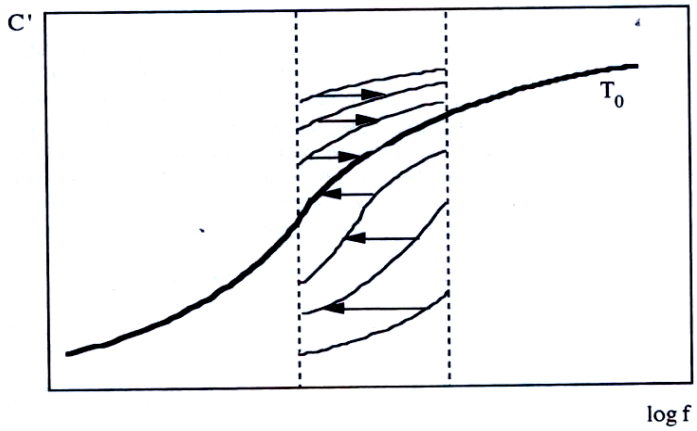

Figure 35 –Shifting the storage modulus curves into a master curve.

The conditions for the applicability of the TTSP are [5]:

- The superposition of the different isothermal curves should result on a unique and smooth curve;

- The function that represents the variation of a_T with the temperature should be continuous and without appreciable flotation's;
- The same function a_T should be able to build the master curves of all the viscoelastic properties.

The master curves were determined using a numerical algorithm developed and implemented by Guedes [47].

4.4.2.2. Empirical power law extrapolation method

Simultaneously DMTA data obtained at 25ºC was reduced to a power law relation. The relaxation modulus was fitted using the following power law:

$$E(t) = E_0 \left(\frac{t}{\tau_0} \right)^n \tag{48}$$

where τ_0 is the reference time, in this case equal to 1 s, and E_0 is the modulus at τ_0. The long-term circumferential modulus was predicted using the previous equation.

4.5. Results

In this section the real-time experimental creep and the DMTA predictions are presented and compared. The objective is to assess the long-term prediction methodologies and the hygrothermal effects due to the preconditioning. Since the material presents rather large initial stiffness variability the experimental data was normalized to the initial circumferential modulus E_i calculated at 0.01hours which corresponds to initial creep deflection.

4.5.1. Creep tests

Unconditioned specimens

The average initial modulus of the unconditioned specimens was 8.96 GPa. The measured circumferential normalized relaxation modulus of some unconditioned specimens is depicted in Figure 36 with the average values.

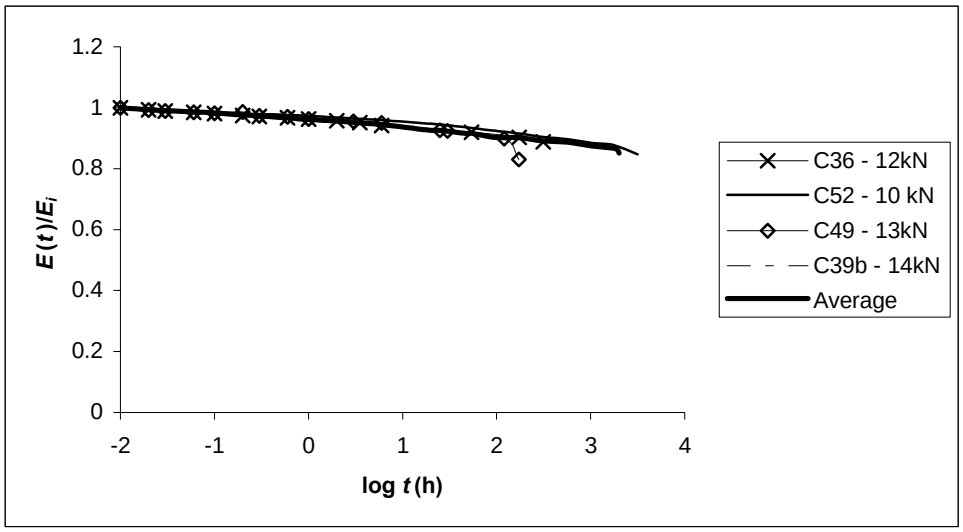

Figure 36 – Circumferential relaxation modulus of unconditioned specimens.

Specimens preconditioned at 50ºC

The average initial circumferential modulus of the preconditioned specimens in water at 50ºC was 8.7GPa. The circumferential normalized relaxation modulus of some specimens preconditioned at 50ºC and tested in water at room temperature is depicted in Figure 37 with the average values.

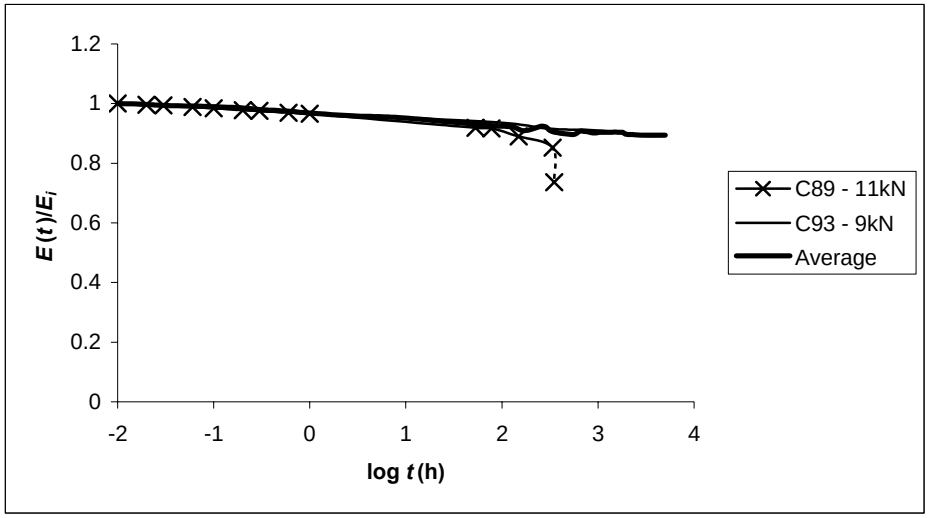

Figure 37 – Circumferential relaxation modulus of preconditioned specimens at 50ºC.

Both unconditioned and preconditioned specimens were tested under the same load and environmental conditions. In Figure 38 is made a comparison of the average normalized relaxation modulus for both cases, unconditioned and preconditioned.

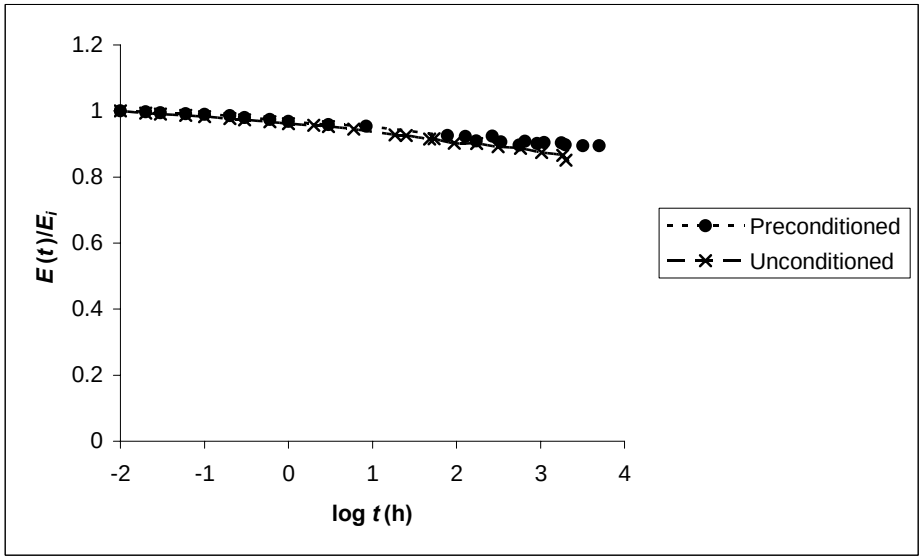

Figure 38 – Comparison of circumferential normalized relaxation modulus (average values) for preconditioned and unconditioned specimens.

4.5.2. DMTA tests

The DMTA data obtained for the type 1 samples was very similar to the specimens type 2. For this reason data distinction was omitted.

The average values of the circumferential instantaneous modulus were determined. E_i is the value of the initial modulus obtained at t=0.01h. The average instantaneous circumferential modulus obtained for the three different cases are presented in Table XVII.

Table XVII – Average instantaneous circumferential modulus (t=0.01h) obtained from DMTA tests.

Specimens	**Unconditioned**	**Water at room temperature**	**Water at 50ºC**
$\boldsymbol{E_i}$ (GPa)	4.34	3.90	3.4

The DMTA results represented by the normalized relaxation modulus are depicted in Figures 39-40.

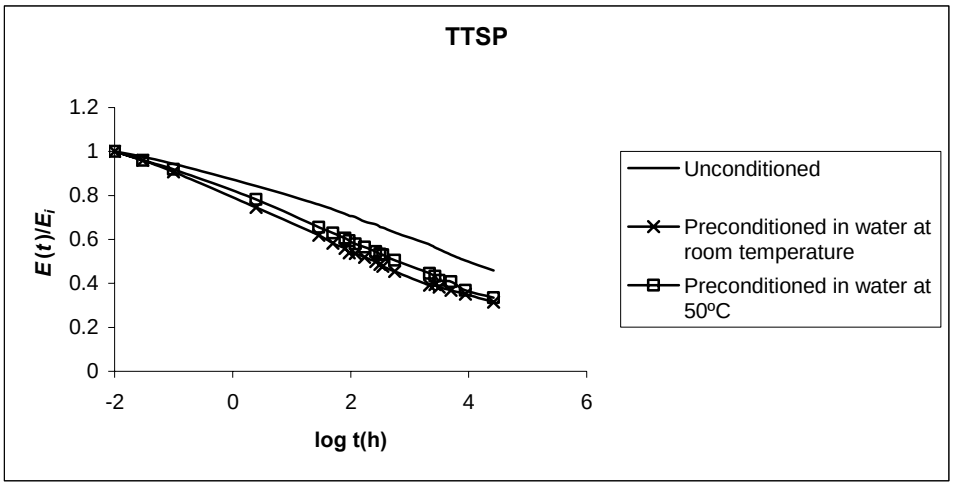

Figure 39 – Circumferential normalized relaxation modulus prediction using TTSP.

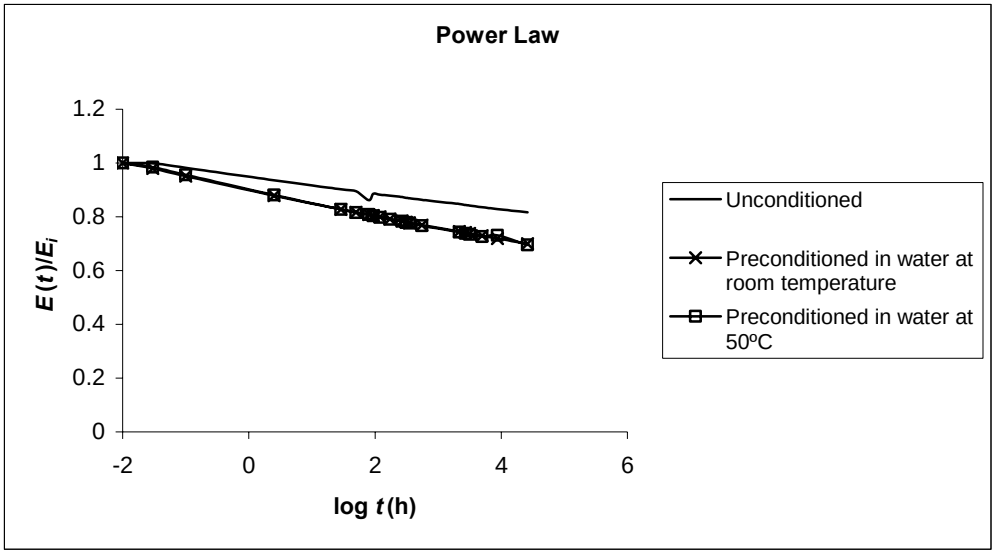

Figure 40 – Circumferential normalized relaxation modulus prediction using power law extrapolation.

In these plots it is possible to observe the differences on both approaches as well as the preconditioning effects. The fitted power law coefficients are presented in Table XVIII.

Table XVIII – Average values of E_0 and n used on power law extrapolation curves.

	Unconditioned		**Water at room temperature**		**Water at 50ºC**	
	E₀	***n***	***E₀***	***n***	***E₀***	***n***
Average	4.658	-0.015	4.281	-0.025	3.773	-0.025
St. dev.	0.679	0.002	0.659	0.002	0.732	0.003

The comparison between the DMTA predictions, based on TTSP and on power law relation, and the creep tests are presented in Figures 41-42.

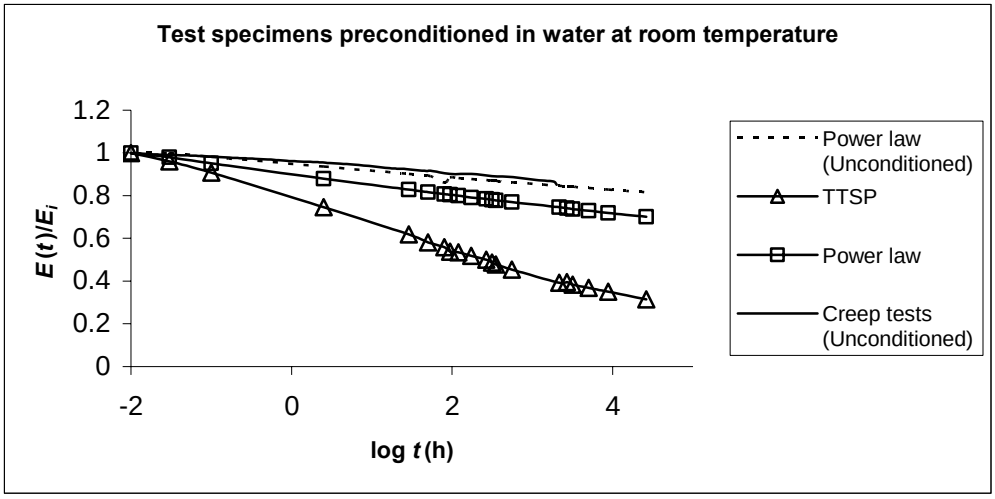

Figure 41 - Comparison between the DMTA results and the creep results.

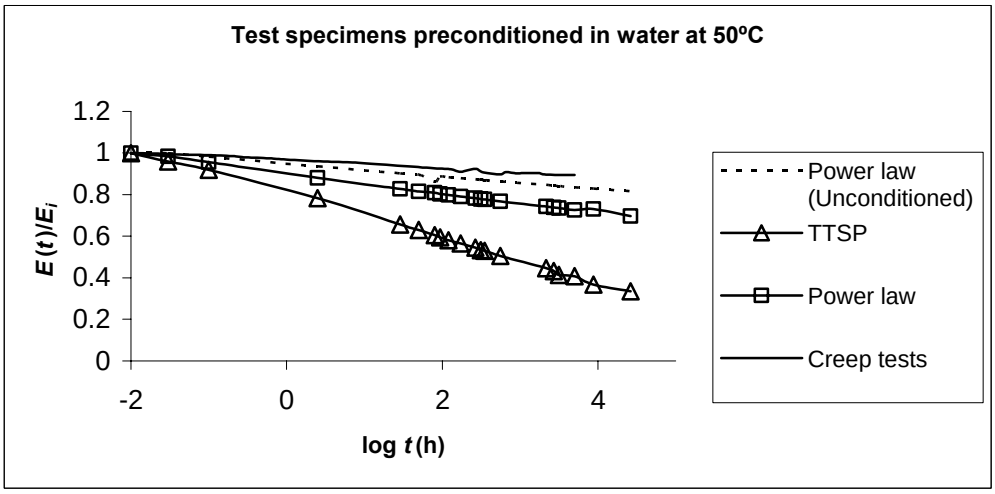

Figure 42 - Comparison between the DMTA results and the creep tests.

4.6. Discussion of results

Both conditioned and unconditioned creep specimens were tested under the same load and environmental conditions. When comparing the average instantaneous modulus (elastic) and the average relaxation modulus depicted in Figure 38 it can be concluded that preconditioning didn't affect significantly the elastic and viscoelastic behaviour.

The DMTA test specimens presented an initial modulus which was approximately half of GRP pipes modulus in the hoop direction. Obviously the structural arrangement of the reinforcements, important in flexural loading, was

broken once these coupons were machined from the pipe. This can explain the stiffness differences. The preconditioning effect on DMTA data was also quite pronounced and the water temperature affected the initial modulus. The explanation for this may lay on the fact that DMTA specimens machined from the pipe didn't include the protective layers which cover the pipes outer surfaces. Still the preconditioning displays an important influence on viscoelastic behaviour, when analysing the normalized relaxation modulus evolution using the power law and TTSP. However the influence of water temperature during preconditioning appears to be negligible. Also the power law coefficients, presented on Table XVIII, show a dependence on the conditioning which confirms its influence on initial modulus and relaxation modulus.

Since the power law extrapolation has shown a good predictive capability, the creep data was also fitted using the same power law. The power law given by Equation 48 was normalized by the initial circumferential modulus E_i calculated at 0.01 hours, as:

$$\frac{E(t)}{E_i} = e_0 \left(\frac{t}{\tau_0} \right)^n \tag{49}$$

where τ_0 is the reference time and e_0 is the modulus fraction at τ_0. In Table XIX are represented the parameters obtained from experimental data.

Table XIX –Coefficients of Equation 49 obtained for the averaged experimental data.

Creep				**DMTA**					
Unconditioned		**Water at 50ºC**		**Unconditioned**		**Water at room temperature**		**Water at 50ºC**	
e_0	n	e_0	n	e_0	n	e_0	n	e_0	n
0.96	-0.012	0.97	-0.0095	0.95	-0.015	0.90	-0.025	0.90	-0.025

Again the power law coefficients show a weak or negligible preconditioning effect on the creep data. However the preconditioning effect on the DMTA

specimens is evident from the coefficients analysis but the water temperature has no visible effect.

The two different methodologies predict quite different relaxation modulus evolution. The TTSP deviates considerably from the power law extrapolation and creep tests as it can be observed in Figures 39-42.

In spite of the differences between the creep tests and DMTA in respect to the test setup and specimen's size, extrapolation using a power law relation based on DMTA data at 25ºC presents quite good predictions for the long-term modulus reduction of pipes.

In Table XX are represented the normalized modulus predicted for 500000 hours using the power law extrapolation given by Equation 49.

Table XX – Long-term normalized modulus extrapolated up to 500000 hours using Equation 49.

Time (h)	Creep		DMTA		
	Uncond.	Water at 50ºC	Uncond.	Water at room temperature	Water at 50ºC
1000	0.879	0.904	0.855	0.759	0.758
10000	0.854	0.884	0.827	0.718	0.716
500000	0.814	0.852	0.782	0.652	0.650

Surprisingly the best approach to the creep data was produced by the unconditioned DMTA test data. It was expected that preconditioned DMTA specimens represented better the creep tests. However the pipes have shown a quite low sensibility to the preconditioning effects on elastic and viscoelastic properties. Certainly the pipe protective layers play an important role in this behaviour. Furthermore the aqueous environment of the creep tests appears to have little influence, since its viscoelastic behaviour is similar to the unconditioned DMTA specimens.

Although the preconditioning water temperature effect, ambient and 50ºC, appeared to be irrelevant some extra phenomena can occur. One phenomenon developed at high temperatures is the post-curing process and the other is the acceleration of the ageing effect. In both cases the outcome would be an increase of

stiffness and strength. However neither these phenomena were taken into account in this study.

4.7. Conclusions

Creep tests were performed on GRP pipes in order to determine the long-term circumferential modulus. It was observed that preconditioning in water at 50ºC had little influence on the initial stiffness of GRP pipes. Furthermore the creep behaviour in aqueous (drinkable water) environment of preconditioned and unconditioned GRP pipes under lateral deflection was quite similar.

Small size specimens cut-out from the GRP pipes were tested on DMTA to be used for long-term mechanical behaviour prediction of GRP pipes. The preconditioning in water at room temperature and at 50ºC displayed a strong influence on the initial stiffness and on the viscoelastic behaviour. However the preconditioning water temperature didn't show any clear influence. The TTSP methodology didn't performed well for long-term modulus prediction, forecasting quite large stiffness decay. However power law relation, fitted to the 25ºC DMTA data, was able to predict with reasonable accuracy the long-term stiffness decay measured by the creep tests that last for 10000 hours. This was achieved in spite of the differences between the two test schemes in terms of loading and size of specimens. Furthermore the reinforcement arrangement was broken when the DMTA samples were cut-out, i.e. the mechanical flexural behaviour became different and the flexural modulus was reduced to half.

Quite surprisingly the power law predictions of long-term creep behaviour of pipes under drinkable water were more accurate when it used the unconditioned DMTA test data. This fact can be related with the protective layers of GRP pipes that were removed when the DMTA samples were cut-out from pipes. Therefore, in this case, moisture influence on mechanical behaviour of GRP pipes appears to be negligible at least during the time span analysed (<10000h). In conclusion, the power law relation displayed a good potential to be used as long-term predictive tool in structural design of GRP structures.

5. Short and long-term failure of GRP pipes

5.1. Introduction

GRP pipes have applications in pressure pipeline as well as in drainage sewerage piping systems. In these applications the pipes are in contact with various fluids that, in some cases may have aggressive effects on the material components of the pipes [8, 20, 50-51]. One of the most important factors which affect the behaviour of these materials is moisture.

During its service life, GRP pipes are submitted to ring deflection creep and quasi-static loading. These loading configurations simulate in laboratory the loads verified in a sub-soil installation. In order to prevent failure of these structures it's very important to know its values of rupture energy and its variation with the loading scheme and with presence of moisture.

Nishizaki [2] studied the effects of water on the durability of pultruded glass-fibre reinforced polymers (GFRP) with vinylester resin for applications in normal air conditions. Deterioration tests, including both immersion and atmosphere conditions at various temperatures, were conducted to investigate the deterioration characteristics of pultruded GFRP after being permeated by water. The bending strength of the GFRP was reduced. The reductions in bending strength were greater in a 60ºC water immersion condition compared to both 60ºC moist-atmosphere condition and a 40ºC water immersion condition.

Farshad [50] performed diametrical compression creep tests on GRP pipes. Prior to creep testing in submerged conditions the samples were conditioned in water at ambient temperature. During the testing period, diametrical deflection of samples was measured and the time to failure of each sample was recorded. The long-term tests showed that, for the pipes tested, the strength corresponding to 1000 testing hours was about 60% of the short-term strength. Moreover, extrapolation of the data to 50 years showed a reduction of strength by about 55%.

In this section the rupture energies and strain at failure of the analysed GRP pipes loaded under short (ring deflection [1] and three-point bending tests) and long-term tests (creep [1]) were determined and compared. The influence of the

preconditioning and loading scheme on failure of GRP pipes was studied. The values of G_{Id} as well as the flexural properties determined for the unconditioned and preconditioned specimens determined on the previous sections were used as input parameters in a finite element model developed by Faria [1] where the damage mechanisms and global mechanics of the GRP pipes can be studied. Thereafter, the influence of the variation induced by moisture on each mechanical property on the failure of the GRP pipes could be assessed. A new range of G_{If}/G_{Id} values was achieved.

5.2. Data reduction schemes

The short and long-term rupture energies and the strain at failure of the GRP pipes tested under different loading conditions (three-point bending (Section 2), creep tests (Section 3) and ring deflection tests [1]) were computed using the data reduction schemes presented in this chapter. The ring deflection tests were performed by Faria [1] according to the European Standard EN1226:1995 [52] used to test the ability of glass reinforced thermosetting plastic pipes to withstand specified levels of initial ring deflection without displaying surface damage and/or structural failure. The ring deflection tests were performed on five specimens with the dimensions described in Figure 28 in a universal INSTRON machine as depicted in Figure 43 where the experimental $P-\delta$ curves were obtained [1].

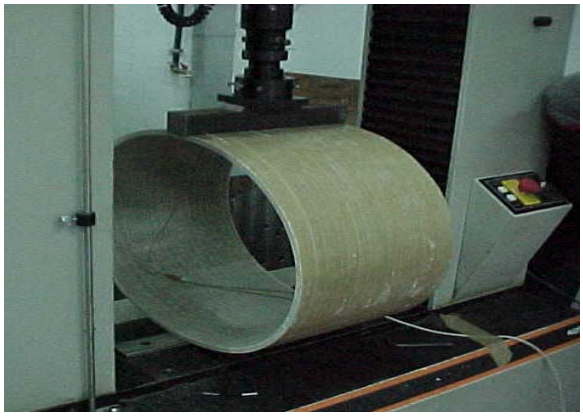

Figure 43 – Ring deflection test apparatus.

In all tests methods (three-point bending, creep and ring deflection tests) failure occurred on the loading section. The fibres subjected to tensile stress fail and

delamination occurs as depicted in Figures 44-45 and on Faria [1]. All the calculations (stresses and strains) performed in this chapter are referred to the point where failure occurs.

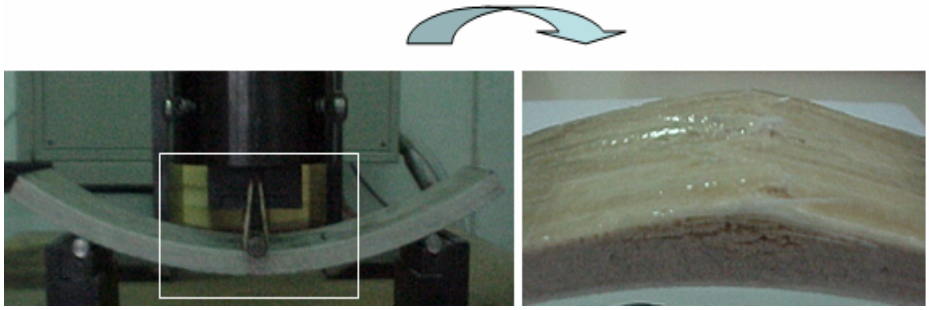

Figure 44 – Delamination on the loading section of a specimen tested in three-point bending with the concave side up.

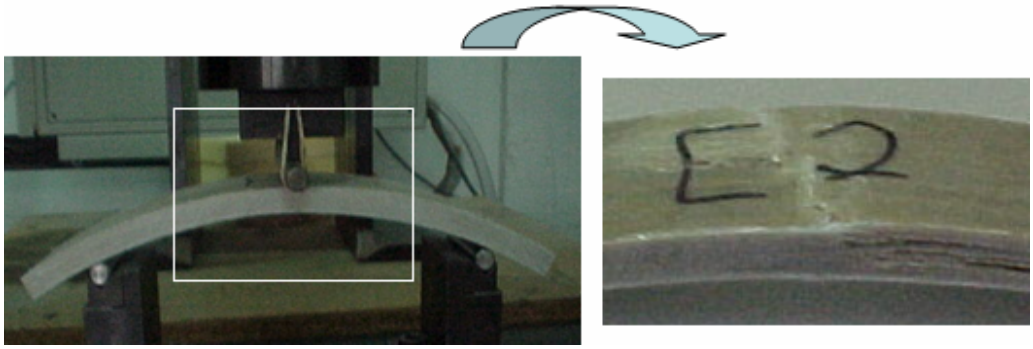

Figure 45 – Delamination on the loading section of a specimen tested in three-point bending with the concave side down.

The strain at failure was computed through Hook's law and the rupture energies were obtained by computing the area under the stress-strain curves obtained on the different loading conditions.

5.2.1. Three-point bending tests on circumferential specimens

Through the values of flexural modulus and ultimate flexural strength obtained on Section 2.5.2 using the Equations 10 and 11 the values of strain (ε) were obtained through the Hook's law (assuming linear elastic behaviour):

$$\sigma = E\varepsilon \tag{50}.$$

The values of rupture energy are given by:

$$Energy_{rupture} = \frac{\sigma_f \times \varepsilon}{2} \tag{51}$$

which is, approximately, the area under the $\sigma = \mathrm{f}(\varepsilon)$ curve.

5.2.2. Ring deflection tests

From the $P-\delta$ curves obtained by Faria [1] and assuming a linear elastic behaviour, the $\sigma-\varepsilon$ curves were obtained and the rupture energies were determined. The maximum hoop stresses on the pipes were obtained using the method proposed on Annex 1 where:

$$\sigma_\theta = \frac{\left(\frac{M\left(ln\left(\frac{R_m + \frac{t}{2}}{R_m - \frac{t}{2}} \right) \right)}{t\left(-t + R_m\, ln\left(\frac{R_m + \frac{t}{2}}{R_m - \frac{t}{2}} \right) \right)} + \frac{N}{t} \right) y + \frac{M}{R_m t} + \frac{N}{t}}{B\left(R_m + y \right)} \tag{52}.$$

On Equation 52 M is the bending moment, N is the axial load, y is the distance in the radial direction from the mid-radius to the point where the stress is to be determined (in this case the outer wall of the pipe), R_m is the medium radius, B is the width and t is the thickness. For the present load case and according to Roark's [34] the axial load is null and the bending moment is given by:

$$M = \frac{PR_m\left(1 - \frac{t^2}{12R_m^2} \right)}{\pi} \tag{53}$$

where P is the applied ring deflection load. The maximum strain was obtained through Equation 50. The values of rupture energy are given by Equation 51.

5.2.3. Creep tests

The experimental data obtained by Faria [1] (ring deflection vs. time) was treated in order to obtain the creep ($\varepsilon(t)$) curves. The values of circumferential modulus and its variation with time were obtained using the presuppositions and Equation 39 of Section 4.4.1. The applied constant hoop stress σ was obtained using Equations 52-53 and the strain ε was obtained through Equation 54.

$$\varepsilon(t) = \frac{\sigma_0}{E(t)} \tag{54}.$$

The rupture energy of a GRP pipe tested in creep is given by the energy of the elastic part plus the energy of the viscoelastic part as described on Equation 55 and Figure 46.

$$Energy_{rupture} = \frac{\sigma \times \varepsilon_{t=0.01h}}{2} + \sigma \times \left(\varepsilon_{t=\infty} - \varepsilon_{t=0.01h}\right) \tag{55}.$$

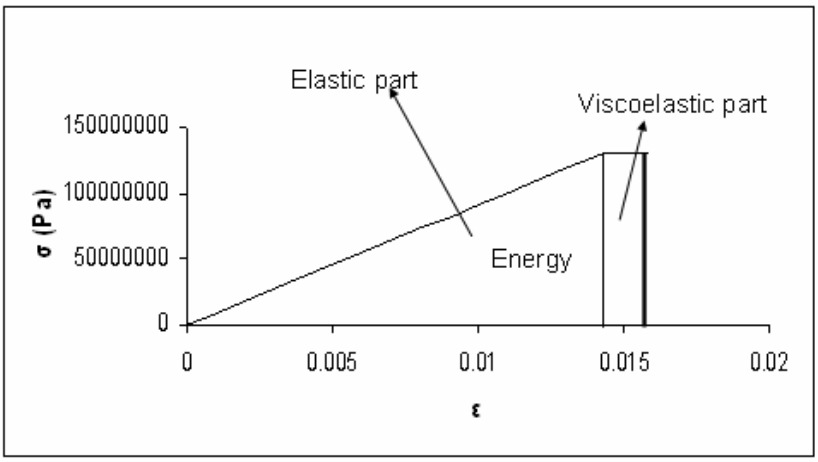

Figure 46 – Energy on creep tests.

5.3. Experimental results

5.3.1. Three-point bending and ring deflection tests

The values of rupture energy and strain at failure obtained for the three-point bending and ring deflection tests [1] are described on Tables XXI-XXII.

The values of rupture energy of the circumferential specimens tested under three-point bending with the concave side up were very similar to the ones obtained for the specimens tested with the concave side down. For this reason data distinction is omitted.

Table XXI – Rupture energy of the three-point bending tests and ring deflection tests.

Rupture energy (MPa)	**Circumferential specimens tested under three-point bending**			**Ring deflection tests**
	Uncond.	**Water at room temperature**	**Water at 50ºC**	**Uncond.**
Medium values	2.909	2.948	2.421	2.794
St. deviation	0.386	0.330	0.203	0.393

Table XXII – Strain at failure of the three-point bending tests and ring deflection tests.

Strain at failure (%)	**Circumferential specimens tested under three-point bending**			**Ring deflection tests**
	Uncond.	**Water at room temperature**	**Water at 50ºC**	**Uncond.**
Medium values	2.382	2.403	2.268	2.297
St. deviation	0.268	0.187	0.119	0.163

5.3.2. Creep tests

The variations of rupture energy and strain at failure with applied stress and with time to failure of the several tested specimens are depicted in Figures 47-

50. The values of ring deflection were measured and registered on certain periods of time [1]. In most cases it wasn't possible to register phase III of creep, i.e. the value of ring deflection immediately before structural failure occurs. Therefore it was considered that the ultimate value of ring deflection was the last one registered before structural failure occurred.

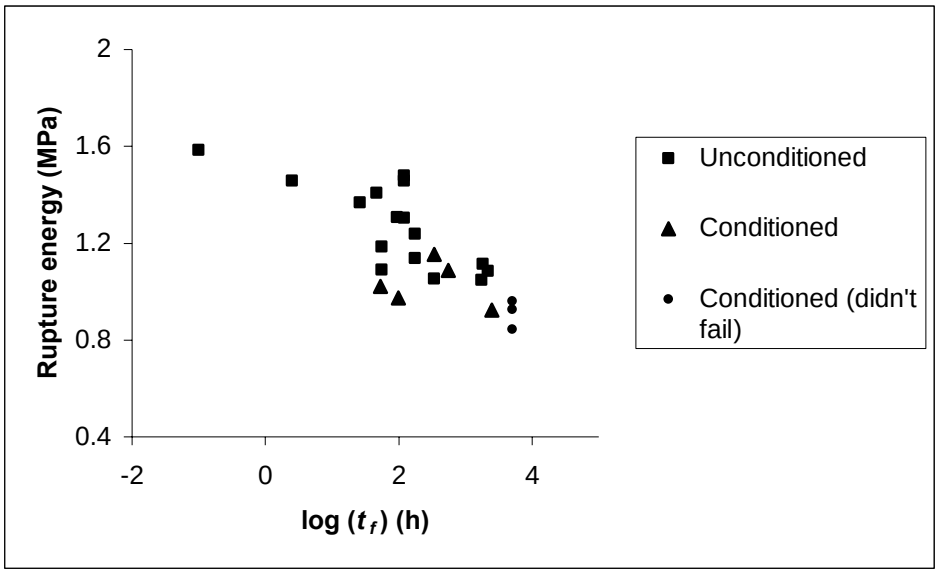

Figure 47 – Rupture energy vs. time to failure.

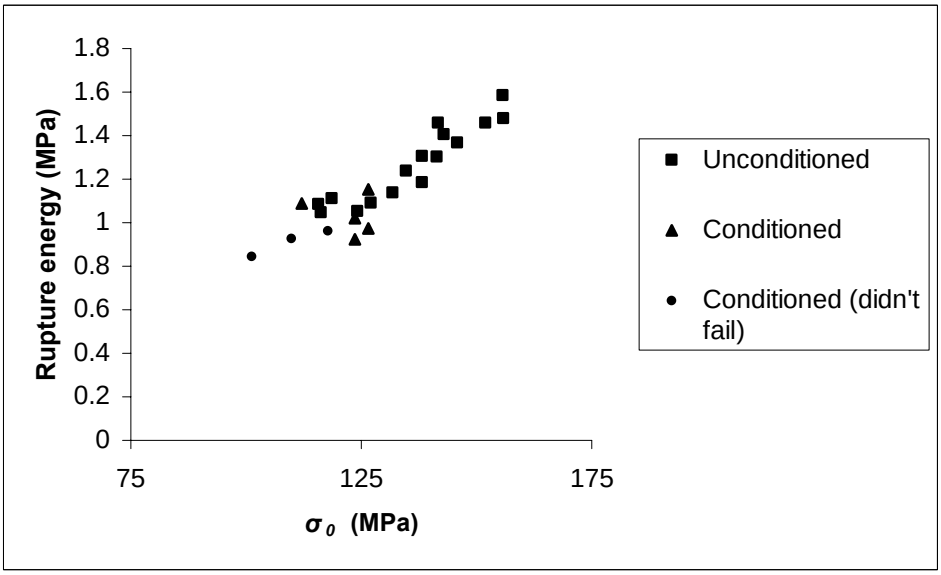

Figure 48 – Rupture energy vs. applied stress.

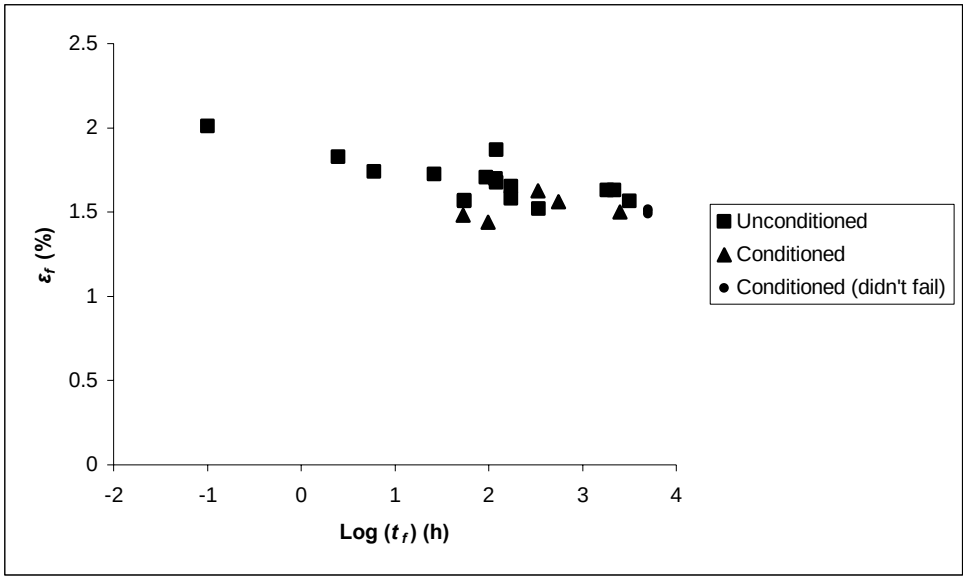

Figure 49 – Strain at failure vs. time to failure.

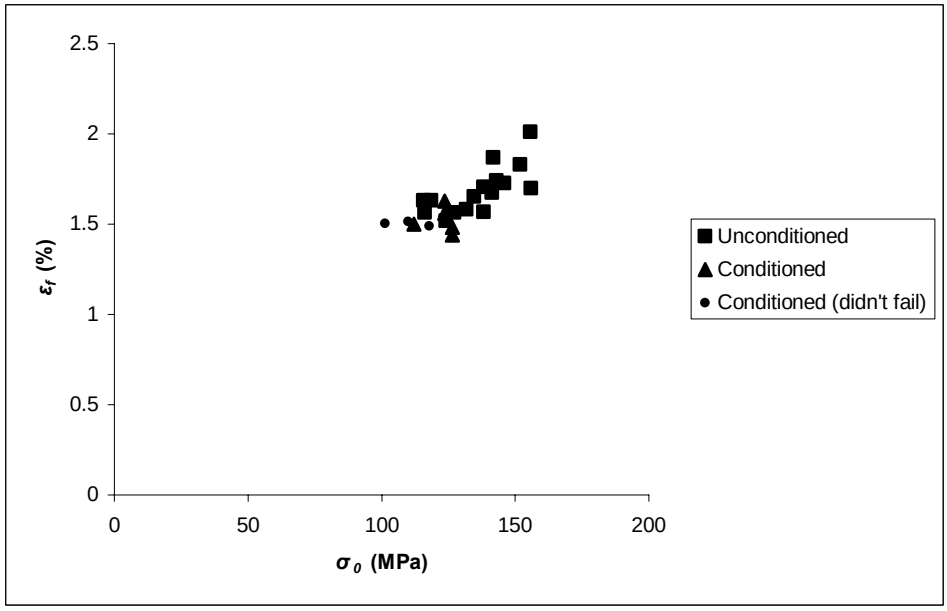

Figure 50 – Strain at failure vs. applied stress.

5.4. Numerical analysis

5.4.1. Numerical models

Faria [1] developed 2D finite element models in order to simulate the damage mechanisms and global mechanics of a GRP pipe under a ring deflected condition. A 2D model was created by Faria [1] based on the geometry and

dimensions depicted in Figure 1 with 10 plies of 1.2mm each, separated by interface cohesive elements allowing simulation of delamination and rupture of fibres, either in mode I and/or mode II [1]. The simulated GRP pipe was represented by a finite element mesh with 9000 quadratic elements (8-node 2D continuum elements CPE8R defined on ABAQUS®) and 8110 interface compatible elements (Section 3.4.1.) disposed along all interfaces as depicted in Figure 51. The ring deflection was imposed by increasing successively the displacement of the loading section (0.2% of ring deflection at each increment) from the initial unloaded condition to the final value specified of 30% ring deflection [1].

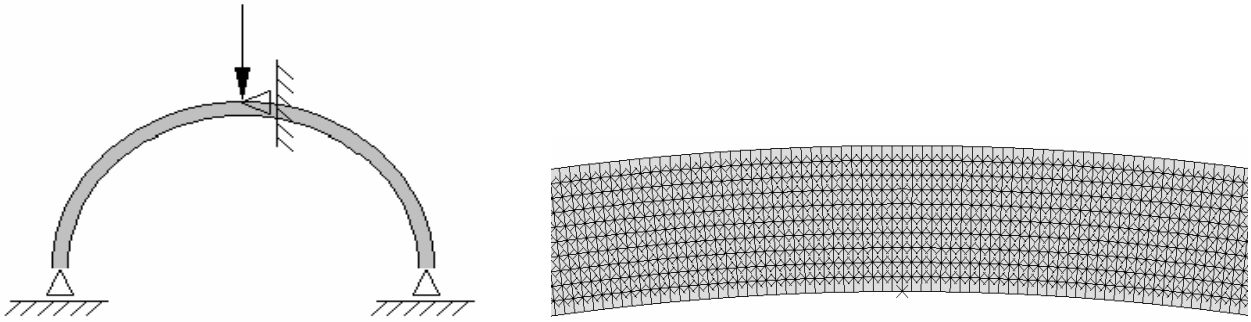

a) b)

Figure 51 – a) Model configuration [1]; b) Detail of the mesh with cohesive elements [1].

Using the G_{Id} values determined on Section 3.3.3 a new G_{If}/G_{Id} ratio was achieved. The influence of moisture on the rupture energy and failure of GRP pipes was studied using the mechanical properties experimentally determined on Sections 2 and 3. Four models with distinct combinations of main parameters were run as depicted on Table XXIII.

Table XXIII – List of examples run.

Model	E_h (MPa)	E_L =E$_R$ (MPa)	υ_{hR}=υ_{hL}	υ_{RL}	G_{hR} =G_{hL} (MPa)	G_{RL} (MPa)	σ_{rup} (MPa)	G_{Id} (kJ/m^2)	G_{If} (kJ/m^2)	G_{IId} (kJ/m^2)
1	10547	3808	0.3	0.4	1000	800	245	0.47	79.9	1.2
2	10547	3808	0.3	0.4	1000	800	245	0.47	47	1.2
3	10547	3808	0.3	0.4	1000	800	245	0.47	14.1	1.2
4	10547	3808	0.3	0.4	1000	800	245	0.22	47	1.2

On Table XXIII E_h is the modulus of the pipe in the hoop direction, E_R is the modulus in the radial direction, E_L is the modulus on the longitudinal direction, σ_{rup} is the rupture stress of the material, G_{Id} is the critical energy release rate for delamination and G_{If} is the critical energy release rate for rupture of fibres.

The first three models (models 1 to 3) were run in order to determine a new G_{If}/G_{Id} ratio. The new G_{If}/G_{Id} ratio was achieved by fitting the numerical P-δ curves to the experimental P-δ curves obtained by Faria [1] on ring deflection tests.

On Section 2 it was seen that the circumferential modulus and ultimate flexural stress of the studied GRP pipes aren't significantly affected by the presence of moisture on the structure of the GRP pipes. Then again, the critical energy release rate for delamination is strongly affected by the presence of moisture on the structure of the pipes as it was seen on Section 3. Therefore, the fourth model described on Table XXIII was run in order to study the influence of the lower values of G_{Id} induced by the presence of moisture on the GRP pipes failure.

5.4.2. Numerical results

The numerical curves ring force vs. ring deflection are presented and compared with the experimental results of ring deflection tests performed by Faria [1] in Figure 52.

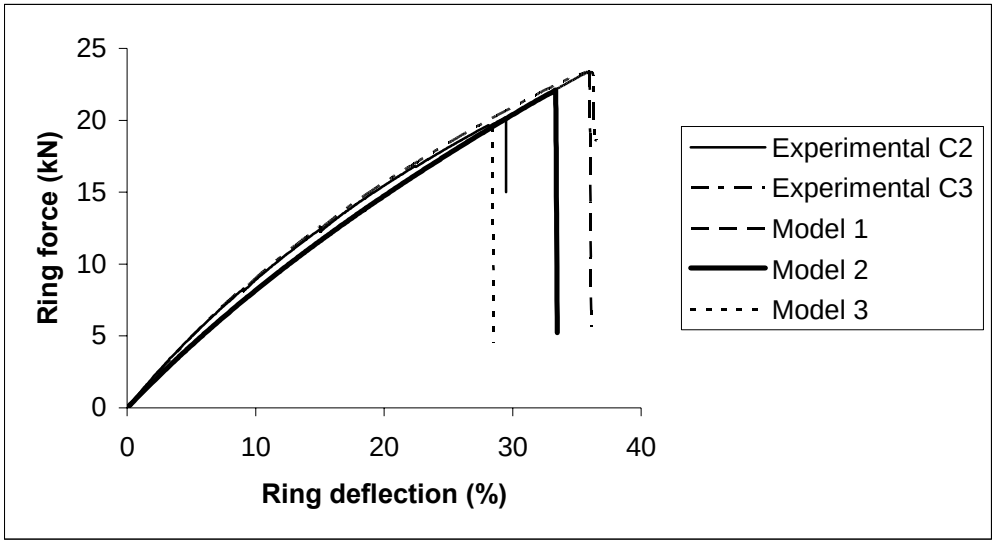

Figure 52 – Fitting the numerical results to the experimental ones.

Through Figure 52 and Table XXIII it is seen that the G_{If} values are in the following ranges:

$$30 \leq \frac{G_{If}}{G_{Id}} \leq 170 \ \frac{\text{kJ}}{\text{m}^2}$$
$$14 \leq G_{If} \leq 80 \ \frac{\text{kJ}}{\text{m}^2} \quad (56).$$

These values are in agreement with the predictions made by Faria [1].

In Figure 53 are depicted and compared the numerical ring force vs. ring deflection curves obtained for model 2 and model 4.

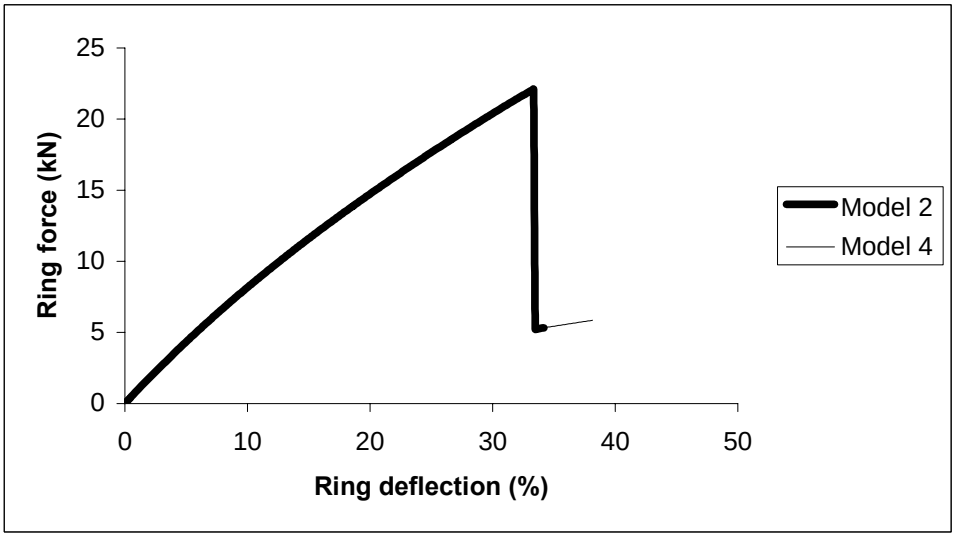

Figure 53 – Influence of G_{Id} on GRP pipes failure.

On Table XXIV are described the rupture energies obtained for the four numerical models.

Table XXIV – Rupture energies of the different models described on Table XXIII.

Model	Rupture energy (MPa)
Model 1	3.210
Model 2	2.870
Model 3	2.247
Model 4	2.870

5.5. Discussion

A high scatter of rupture energies and strain at failure was obtained as it is seen on Tables XXI-XXII and Figures 47-50.

The rupture energies and strain at failure of the circumferential specimens tested in three-point bending are very similar to the ones obtained for the ring deflection tests, as it was expected. On the circumferential specimens saturated in water at 50ºC it is seen a lowering on the average values of rupture energy and strain at failure. However due to the high scatter measured one cannot say confidently that the saturation with water at 50ºC promotes significant reductions on the values of rupture energy and strain at failure.

Failure of GRP pipes subjected to long-term load application occurs at lower levels of energy and strain in comparison with the ones subjected to quasi-static loads as it can be seen in Figures 47-50 and Tables XXI-XXII. The values of rupture energy of the specimens tested in creep are about 50% of the ones tested under quasi-static loads. Due to the lower levels of applied stress on creep tests the damage (rupture of fibres) has more time to accumulate and propagate than in quasi-static tests. On creep tests the load was applied with the specimens submerged in water and the combined effects moisture/load is expected to have a more pernicious effect on the material. These phenomena can explain the decrease of rupture energies and strain at failure occurred during creep tests.

As depicted in Figure 54 the energy at failure decreases with creep time and is well fitted by a power law.

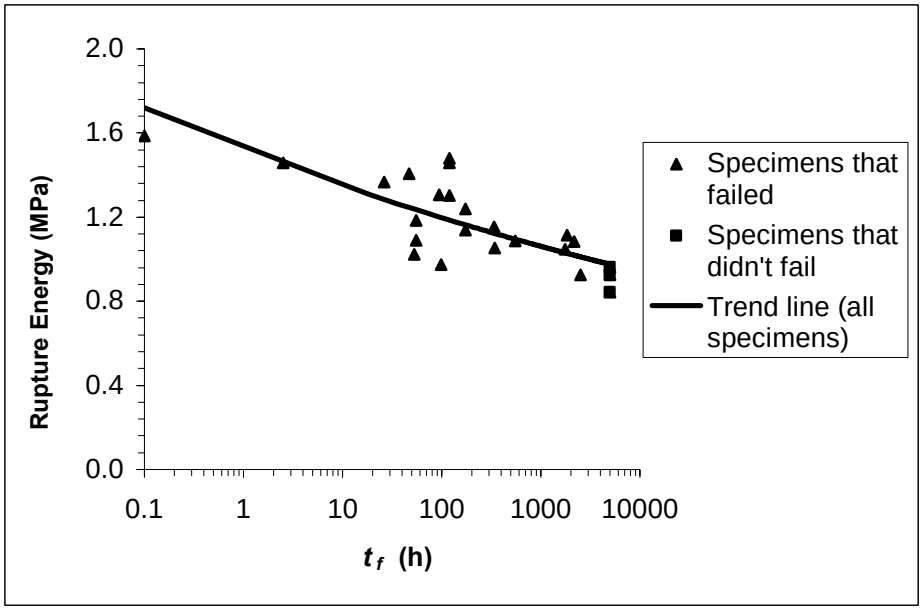

Figure 54 – Rupture energy vs. time to failure.

The only analysed property that was significantly affected by the preconditioning was G_{Id}. In Figure 53 and Table XXIV it was seen that the numerical ring force vs. ring deflection curves and rupture energies of models 2 and 4 are coincident. So, the critical energy release rate for delamination doesn't influence the load and deflection at rupture of the analysed pipes.

Moisture doesn't have a significant influence on failure of the analysed GRP pipes.

5.6. Conclusions

Rupture energy and strain at failure were determined on GRP pipes tested under several loading and preconditioning conditions. In all tests methods (three-point bending, creep [1] and ring deflection tests [1]) failure occurred on the section where the load was applied. The fibres subjected to tensile stress fail and delamination occurs as depicted in Figures 44-45 and on Faria [1]. A numerical model performed by Faria [1] was used to study the influence of moisture on failure of the analysed GRP pipes.

The rupture energies and strain at failure of the circumferential specimens tested in three-point bending are very similar to the ones obtained for the ring deflection tests. Failure of GRP pipes subjected to long-term loads occur at lower levels of

energy and strain in comparison with the ones subjected to quasi-static loads. The values of rupture energy of the specimens tested in creep are about 50% of the ones tested under quasi-static loads.

The reduction induced by the preconditioning on the values of critical energy release rate for delamination (Section 3) doesn't influence the load and deflection at rupture of the analysed GRP pipes. It can be concluded that the preconditioning in moisture doesn't have a significant influence on failure of GRP pipes.

6. Conclusions of the work

In this study several experimental and numerical procedures were accomplished in order to assess the influence of moisture on quasi-static and long-term failure of GRP pipes.

The influence of moisture on the flexural properties of GRP pipes was assessed by performing three-point bending tests on circumferential and longitudinal specimens. A more accurate data reduction scheme was studied and proposed in order to determine the flexural modulus and ultimate flexural strength of curved specimens. A high scatter was measured. The conditioning in water at 50ºC promotes a lowering on the values of flexural modulus on the longitudinal direction of about 30%. However due to the high scatter measured one cannot say confidently that moisture promotes significant reductions of circumferential modulus and ultimate flexural strength. The one-dimensional Fick's law is quite reliable to predict the moisture absorption process in this kind of material.

The critical energy release rate for delamination G_{Id} was determined for unconditioned and preconditioned specimens machined from the circumferential direction of GRP pipes. Moisture has a very pronounced influence on the values of G_{Id}. The critical energy release rate for delamination of the unconditioned specimens is about 0.47 N/mm and for the preconditioned ones is 0.22 N/mm. The temperature of the preconditioning does not influence the values of G_{Id}.

The TTSP and an empirical power law relation were applied to DMTA data of unconditioned and preconditioned specimens machined from the circumferential direction of GRP pipes. The long-term modulus predictions performed with these techniques were compared with real-time creep data [1] of unconditioned and preconditioned specimens. The TTSP methodology didn't performed well for long-term modulus predictions forecasting large stiffness decay. In spite of the differences between the creep and DMTA tests in respect to the test setup and specimen's size, the power law relation fitted to the 25ºC DMTA data was able to predict with reasonable accuracy the long-term stiffness decay measured by the creep tests [1] that last 10,000 hours. The power law relation displayed a good potential to be used as a long-term predictive tool in structural design of GRP structures.

Through the experimental three-point bending, ring deflection [1] and creep data [1] the short and long-term rupture energies and strain at failure were determined and compared. In all test methods failure occurred on the section where the load was applied. Failure of GRP pipes submitted to long-term loading conditions occurs at lower levels of energy (50%) and strain compared with quasi-static load application. This can be explained through different damage propagation times, which naturally depend on the test duration. The influence of the preconditioning in moisture on failure behaviour of the analysed GRP pipes is not very significant.

7. References

[1] Faria, H.Q.; “Failure analysis of GRP pipes Under Compressive Ring Loads”, Master thesis, Faculdade de Engenharia da Universidade do Porto, 2005;

[2] Nishizaki, I.; Meiarashi, S.;”Long-Term Deterioration of GFRP in Water and Moist Environment”, Journal of Composites for Construction, 2002, 6 (1): 21-27;

[3] Perreux, D.; Suri, C.; “A Study of the Coupling between the Phenomena of Moisture Absorption and Damage in Glass/Epoxy Composite Pipes”, Composites Science and Technology, 1997, 57:1403-1413;

[4] Ghorbel, I.; Spiteri, P.; “Durability of Closed-End Pressurized GRP Pipes under Hygrothermal Conditions. Part I: Monotonic Tests”, Journal of Composite Materials, 1996, 30 (14):1562-1580

[5] Morais, J. J. L.;”Influência do Meio Ambiente no Comportamento ao Dano de Estruturas em Materiais Compósitos” Phd Thesis, Universidade de Trás-os-Montes e Alto Douro, 1998;

[6] Bond, D. A.; ”Moisture Diffusion in a Fibre-Reinforced Composite: Part I- Non-Fickian Transport and the Effect of Fibre Spatial Distribution”, Journal of Composite Materials, 2005, 39(23):2113- 2141;

[7] Kouadio, K. S. P.; “Durability of Fibreglass Composite Sheet Piles in Water”, Master Thesis, McGill University, Canada, 2001;

[8] Kootsookos, A.; Mouritz, A.P.;”Seawater Durability of Glass- and Carbon-Polymer Composites”, Composites Science and Technology, 2004, 64:1503-1511;

[9] Ellyin, F.; Maser, R.; “Environmental Effects on the Mechanical Properties of Glass-Fibre Epoxy Composite Tubular Specimens”, Composites Science and Technology, 2004, 64:1863-1874;

[10] Tompkins, S. S.; “Analysis of Moisture Absorption and Diffusion in Fiber Reinforced Polymeric Resin-Matrix Composite Materials”, PhD Thesis, University of Virginia, 1968;

[11] Shen, C. H., Springer, G. S.; ”Moisture Absorption and Desorption of Composite Materials”, Journal of Composite Materials, 1976, 10:2-20;

[12] Pierron, F.; Poirette, Y.; Vautrin,A.; “A Novel Procedure for Identification of 3D Moisture Diffusion Parameters on Thick Composites: Theory, Validation and Experimental Results”, Journal of Composite Materials, 2002, 36 (19):2219-2243;

[13] Crank, J.;”The Mathematics of Diffusion”, Oxford Science Publications, Clarendon Press, 1956;

[14] Kumosa, L.; Armentrout, B.; “An Investigation of Moisture and Leakage Currents in GRP Composite Hollow Cilinders”; IEEE Transactions on Dielectrics and Electrical Insulation, 2005, 12 (5):1043-1059;

[15] Kumosa, L.; Benedikt, B.; “Moisture Absorption Properties of Unidirectional Glass/Polymer Composites used in Composite (Non-Ceramic) Insulators” Composites: Part A, 2004, 35:1049-1063;

[16] Roy, S.; Xu, W.X.; Park, S.J.; “Anomalous Moisture Diffusion in Viscoelastic Polymers: Modelling and Testing”, Journal of Applied Mechanics, 2000, 67:391-396;

[17] Maggana, C.; Pissis, P.; “Water Sorption and Diffusion Studies in an Epoxy Resin System”, Journal of Polymer Science: Part B: Polymer Physics, 1999, 37:1165-1182;

[18] Cai, L.W., Weistman, Y.; “Non-Fickian Moisture Diffusion in Polymeric Composites” Journal of Composite Materials, 1994, 28 (2):130-154;

[19] Raghavan, J.; Meshii, M.; “Creep Rupture of Polymer Composites”, Composites Science and Technology, 1997, 57:375-388;

[20] Akay, M.; Mun, S.K.A.; Stanley, A.; “Influence of Moisture on the Thermal and Mechanical Properties of Autoclaved and Oven-Cured Kevlar-49/Epoxy Laminates”; Composites Science and Technology, 1997, 57:565-571;

[21] Standard ISO 14125, “Fibre-reinforced Plastic Composites – Determination of Flexural Properties”, 1998;

[22] Ozdil, F., Carlsson, “Characterization of Mixed Mode Delamination Growth in Glass/Epoxy Composite Cylinders”, Journal of Composite Materials, 2000, 34 (5):420-442;

[23] Ozdil, F., Carlsson, L.A., LI, X., “Characterization of Mode II Delamination Growth in Glass/Epoxy Composite Cylinders”, Journal of Composite Materials, 2000, 34 (4):274-298;

[24] Srivastana, V. K.; Hogg, P.J. “Moisture Effects on the Toughness, Mode-I and Mode-II of Particles Filled Quasi-Isotropic Glass-Fibre Reinforced Polyester Resin Composites”, Journal of Materials Science, 1998, 33:1129-1136;

[25] Zenasni, R., et al; “Effect of Hygrothermomechanical Aging on the Interlaminar Fracture Behaviour of Woven Fabric Fibre/PEI Composite Materials” Journal of Thermoplastic Composite Materials, 2006, 19:385-398;

[26] Khayankarn, O.; Pearson, R. A.; Verghese, N.; Shafi, A.; “Strength of Glass/Epoxy Interfaces After Hygrothermal Aging”, The Journal of Adhesion, 2005, 81:941-961;

[27] Chou, I.; “Effect of Fibre Orientation and Moisture Absorption on the Interlaminar Fracture Toughness of CFRP Laminates”; Adv. Composite Mater., 1998, 7(4):377-394;

[28] Asp, L.E.;”The Effects of Moisture and Temperature on the Interlaminar Delamination Toughness of a Carbon/Epoxy Composite”; Composites Science and Technology, 1998, 58:967-977;

[29] Selzer, R.; Friedrich, K.; ”Mechanical Properties and Failure Behaviour of Carbon Fibre-Reinforced Polymer Composites Under the Influence of Moisture”; Composites Part A, 1997, 28A:595-604;

[30] Standard ISO/DIS 15024, “Determination of Mode I interlaminar fracture toughness, GIc, for unidirectionally reinforced materials”, 1999;

[31] Gonçalves, J.P.M., Moura, M.F.S.F., Castro, P.M.S.T and Marques, A.T., “Interface element including point-to-surface constraints for three-dimensional problems with damage propagation”, Engineering Computations: Int. J. Comp. – Aided Eng. Software, 2000, 17:28-47;

[32] Silva, M.A.L., de Moura, M.F.S.F., Morais, J.J.L., “Numerical analysis of the ENF test for Mode II wood fracture”, Composites Part A, 2005, In Press

[33] Silva, M.A.L., de Moura, M.F.S.F, Morais, J.J.L., “Análise por elementos finitos do ensaio DCB de juntas coladas com madeira”, 4as jornadas politécnicas de Engenharia, ISEP Porto 2004, pp.437-446;

[34] Young, Warren C., Budynas, R. G., “Roark’s Formulas for Stress and Strain”, 6th Edition, McGraw-Hill, 2002;

[35] De Moura, M.F.S.F, Gonçalves, J.P.M., Marques, A.T., De Castro, P.M.S.T., “Modeling Compression Failure after Low Velocity Impact on Laminated Composites Using Interface Elements”, Journal of Composite Materials, 1997, 31(15):1462-1479;

[36] Julius, M. J.; “Time, Temperature and Frequency Viscoelastic Behaviour of Commercial Polymers”; MSc Thesis, West Virgínia University, 2003

[37] Wang, J. Z.; Parvatareddy, H.; Chang, T.; Physical Aging Behaviour of High-Performance Composites”; Composites Science and Technology, 1995, 54:405-415;

[38] Yao, J.; Ziegman, G.;” Equivalence of Moisture and Temperature in Accelerated Test Method and its Application in Prediction of Long-Term Properties of Glass-Fibre Reinforced Epoxy Pipe Specimen”; Polymer Testing, 2006, 25:149-157;

[39] Barbero, E. J.; Julius, M.J.; “Time-Temperature-Age Viscoelastic Behaviour of Commercial Polymer Blends and Felt Filled Polymers”, Mechanics of Advanced Materials and Structures, 2004, 11:287-300;

[40] Feng, C. W.; Keong, C. W.; Hsueh, Y. P.; “Modeling of Long-Term Creep Behaviour of Structural Epoxy Adhesives”; International Journal of Adhesion & Adhesives, 2005, 25:427-436;

[41] Chen, M.;”Accelerated Viscoelastic Characterization of E-Glass/Epoxy Composite”; PhD Thesis, Northwestern University, 1991;

[42] Goertzen, W. K.; Kessler, M. R.; “Creep Behaviour of Carbon Fibre/Epoxy Matrix Composites”; Materials Science and Engineering A, 2006, 421:217-225;

[43] Miyano Y., Nakada M.; “Accelerated Testing for Long-Term Durability of FRP Laminates for Marine Use”; Journal of Composite Materials, 2005, 39(1):5-20;

[44] Diggwa A.D.S.; Norman, R.H. “Mechanism of Creep of GRP: 2. Microfailures”; RAPRA, 1997, Research Report 194;

[45] EN 1227, CEN, December 1997;

[46] Polymer Laboratories. Dynamic Mechanical Thermal Analyser;

[47] Guedes R.M., Marques A.T., Cardon A.; "Creep or Relaxation Master Curves Calculated from Experimental Dynamic Viscoelastic Function"; Science and Engineering of Composite Materials; 1998, 7(3):259-267;

[48] Findley W.N.; Lai J.S.; Onaran K.;"Creep and Relaxation of Nonlinear Viscoelastic Materials"; Dover Publications, New York; 1989;

[49] Park S.W.; Kim Y.R.;"Interconversion between relaxation modulus and creep compliance for viscoelastic solids"; Journal of Materials in Civil Engineering, 1999, 11(1):76-82;

[50] Farshad, M.; Necola, A.;"Effect of Aqueous Environment on the Long-Term Behaviour of Glass Fiber-Reinforced Plastic Pipes"; Polymer Testing, 2004, 23:163-167;

[51] Liao, K.; Tan, Y.;"Influence of Moisture-Induced Stress on In Situ Fiber Strength Degradation of Unidirectional Polymer Composite"; Composites: Part B, 2001, 32:365-370;

[52] EN1226, CEN, 1995;

[53] Ragab, A.; Bayoumi, S.E.;"Engineering Solid Mechanics: Fundamentals and applications"; CRC Press, 1999;

[54] Lim, C.W.; Wang, C.M.; Kitipornchai, S.; "Timoshenko Curved Beam Bending Solutions in Terms of Euler-Bernoulli Solutions", Archive of Applied Mechanics, 1997, 67:179-190;

[55] Madureira, L.; "Problemas de Equações Diferenciais Ordinárias e Transformadas de Laplace", FEUP Edições, 1ª Edição, 2000;

[56] Lin, S.M.; "Exact Solutions for Extensible Circular Curved Timoshenko Beams with Nonhomogeneous Elastic Boundary Conditions", Acta Mechanica, 1998, 130:67-79;

8. Annex

Annex 1 – Data reduction scheme based on thin curved beam theory;

Annex 2 – Study of the applicability of the data reduction schemes applied to flexural tests of curved beams;

Annex 1

Data reduction scheme based on thin curved beam theory

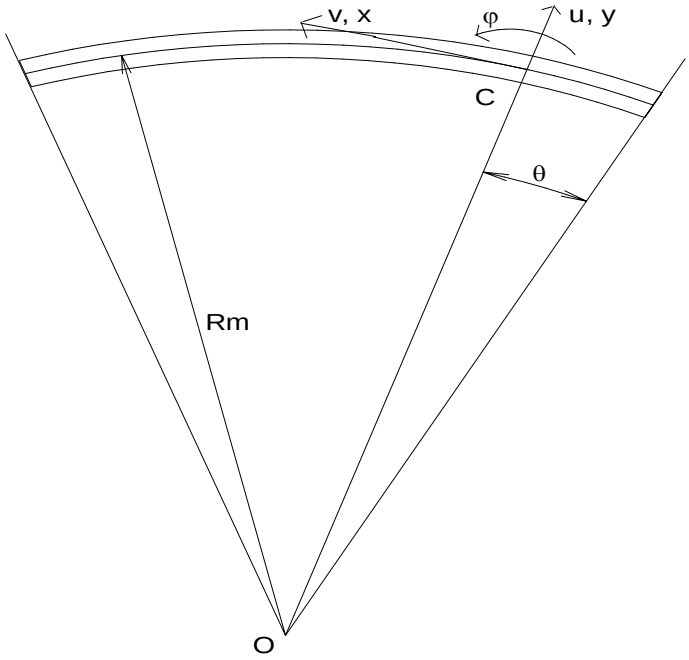

Figure 55 – Thin curved beam.

The relations between strain and displacements in polar coordinates with $r = R_m + y$ are [53]:

$$\varepsilon_\theta = \frac{u(\theta)}{r} + \left(\frac{\frac{\partial}{\partial \theta} v(\theta, y)}{r} \right)$$
$$\varepsilon_{r,\theta} = \frac{\frac{\partial}{\partial \theta} u(\theta)}{r} + \left(\frac{\partial}{\partial y} v(\theta, y) \right) - \frac{v(\theta, y)}{r} \tag{57}$$

where u and v are, respectively, the radial and tangential displacement of the centroid of the section and φ is the rotation of the transverse section. The parameters u, v and φ

define the displacement of the section on θ and are given in function of θ. At any section point the displacements are given by:

$$\begin{aligned} u(\theta) &= u_0(\theta) \\ v(\theta, y) &= v_0(\theta) + \varphi y \end{aligned} \tag{58}$$

where $u_0(\theta)$ and $v_0(\theta)$ are, respectively, the radial and tangential displacement of the medium line. Then:

$$\begin{aligned} \varepsilon_\theta &= \frac{u_0(\theta)}{R_m + y} + \frac{\frac{\partial}{\partial\theta} v_0(\theta)}{R + y} \\ \gamma_{r\theta} &= \frac{\left(\frac{\partial}{\partial\theta} u_0(\theta)\right) + \varphi R_m - v_0(\theta)}{R_m + y} \end{aligned} \tag{59}.$$

The strain ε_θ becomes [54]:

$$\varepsilon_\theta = \frac{R_m}{R_m + y}(\varepsilon + y\kappa) \tag{60}$$

where the curvature κ is given by [54]:

$$\kappa = \frac{\partial\varphi}{R_m \partial\theta} \tag{61}.$$

By assuming zero shear strain ($\gamma_{r\theta}$=0), φ and κ can be determined in function of u and v, as follows:

$$\begin{aligned} \varphi &= -\frac{\left(\frac{\partial}{\partial\theta} u_0(\theta)\right) - (v_0(\theta))}{R_m} \\ \kappa &= -\frac{\left(\frac{\partial^2}{\partial\theta^2} u_0(\theta)\right) - \left(\frac{\partial}{\partial\theta} v_0(\theta)\right)}{R_m} \end{aligned} \tag{62}.$$

By assuming that the material is linear elastic (obeys Hook law) and neglecting the effects of σ_r on the computation of ε_θ , σ_θ becomes:

$$\sigma_\theta = E\varepsilon_\theta = \left(\frac{ER_m}{R_m + y}\right)\left(\varepsilon_\theta + \kappa y\right) \tag{63}.$$

The axial force and the bending moment are given by [53]:

$$\begin{aligned} N &= \int_A \sigma_\theta dA = \int_A E\frac{R_m}{R_m + y}\left(\varepsilon + \kappa y\right)dA = E\varepsilon\int_A \frac{R_m}{R_m + y}dA + E\kappa\int_A \frac{R_m y}{R_m + y}dA \\ M &= \int_A y\sigma_\theta dA = \int_A E\frac{R_m y}{R_m + y}\left(\varepsilon + \kappa y\right)dA = E\varepsilon\int_A \frac{R_m y}{R_m + y}dA + E\kappa\int_A \frac{R_m y^2}{R_m + y}dA \end{aligned} \tag{64}.$$

For a rectangular cross section (Figure 56 where *t* is the thickness), integrating Equation 64, κ and ε becomes:

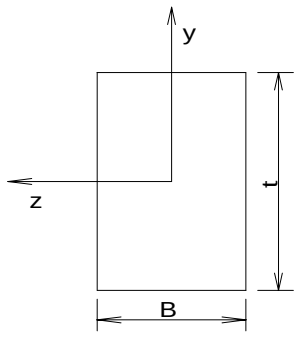

Figure 56 – Rectangular cross section.

$$\begin{aligned} \kappa &= \frac{ln\left(\dfrac{R_m + \dfrac{t}{2}}{R_m - \dfrac{t}{2}}\right)M}{ER_mBt\left(R_m\, ln\left(\dfrac{R_m + \dfrac{t}{2}}{R_m - \dfrac{t}{2}}\right) - t\right)} + \frac{N}{ER_mBt} \\ \varepsilon &= \frac{M}{ER_mBt} + \frac{N}{EBt} \end{aligned} \tag{65}.$$

Combining Equation 65 with Equation 63 σ_θ becomes:

$$\sigma_\theta = \frac{\left(\frac{M\left(ln\left(\frac{R_m + \frac{t}{2}}{R_m - \frac{t}{2}} \right) \right)}{t\left(-t + R_m\, ln\left(\frac{R_m + \frac{t}{2}}{R_m - \frac{t}{2}} \right) \right)} + \frac{N}{t} \right) y + \frac{M}{R_m t} + \frac{N}{t}}{B\left(R_m + y\right)} \tag{66}$$

where M and N are, respectively, the bending moment and the axial force.

In order to determine the equations of bending moment, axial force and transverse force the equilibrium differential equations [53, 54] in polar coordinates were used and are given by:

$$\begin{aligned} \left(\frac{\partial}{\partial\theta} N(\theta)\right) + Q(\theta) &= 0 \\ \left(\frac{\partial}{\partial\theta} Q(\theta)\right) - N(\theta) &= 0 \\ \left(\frac{\partial}{\partial\theta} M(\theta)\right) - R_m Q(\theta) &= 0 \end{aligned} \tag{67}.$$

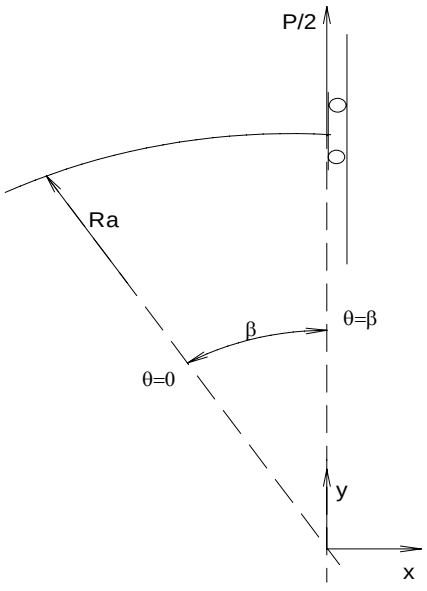

Figure 57 – Curved beam scheme.

$$\sum F^{y} = 0 \Rightarrow R_a \cos(\beta) = \frac{P}{2} \Rightarrow R_a = \frac{P}{2\cos(\beta)} \tag{68}$$

The differential equations of equilibrium follows:

$$\begin{cases} \dfrac{\partial}{\partial\theta} N(\theta) = -Q(\theta) \\ \dfrac{\partial^2 Q(\theta)}{\partial\theta^2} - \dfrac{\partial N(\theta)}{\partial\theta} = 0 \end{cases} \Rightarrow \begin{cases} \dfrac{\partial^2 Q(\theta)}{\partial\theta} + Q(\theta) = 0 \end{cases} \tag{69}$$

By solving the homogeneous equation [55] the transverse force becomes:

$$Q = C_1 \cos(\theta) + C_2 sen(\theta) \tag{70}$$

Inserting the boundary conditions (Equation 71) on Equation 70:

$$\begin{aligned} \theta = 0 &\Rightarrow Q = \frac{P}{2\cos(\beta)} \\ \theta = \beta &\Rightarrow Q = \frac{P}{2} \end{aligned} \tag{71}$$

then:

$$Q = \frac{P}{2\cos(\beta)} \cos(\theta) \tag{72}$$

Through Equation 72 and from the equilibrium equations described on Equation 67 the equations of the bending moment and transverse force were obtained:

$$\begin{aligned} M &= -\frac{PR_m sen(\theta)}{2\cos(\beta)} \\ N &= -\frac{Psen(\theta)}{2\cos(\beta)} \end{aligned} \tag{73}$$

For the calculation of the differential equation of displacements the following relations were used:

$$\varepsilon_\theta = \frac{1}{R_m}\left(u + \frac{\partial v(\theta)}{\partial\theta}\right) = \frac{1}{EA}\left(N + \frac{M}{R}\right)$$
$$\kappa = \frac{\partial\varphi}{R_m\partial\theta} = \frac{M}{EI'} + \frac{1}{EAR_m}\left(N + \frac{M}{R}\right)$$
$$\varphi = \frac{1}{R_m}\left(v - \frac{\partial u}{\partial\theta}\right) \qquad (74).$$
$$\text{where } I' = AR_m^2 z,\ z = \frac{R_m}{t} ln\left(\frac{R_m + \frac{t}{2}}{R_m - \frac{t}{2}}\right) - 1 \text{ and } A = Bt$$

The solution of Equation 74 then gave:

$$v = \left(\frac{\partial}{\partial\theta} u_0(\theta)\right) + \varphi R_m$$
$$\varphi = \int \kappa\partial\theta . R_m = \left(\frac{\left(ln\left(R_m + \frac{t}{2}\right) - ln\left(R_m - \frac{t}{2}\right)\right)M}{ER_m Bt\left(-t + R_m\, ln\left(R_m + \frac{t}{2}\right) - R_m\, ln\left(R_m - \frac{t}{2}\right)\right)} + \frac{N}{ER_m Bt}\right)\theta R_m \qquad (75).$$

Through Equations 74 and 75 it is possible to obtain the differential equation of the displacements for y=0.

$$\left(\frac{ln\left(\frac{R_m + \frac{t}{2}}{R_m - \frac{t}{2}}\right)}{EBt\left(-t + R_m\, ln\left(\frac{R_m + \frac{t}{2}}{R_m - \frac{t}{2}}\right)\right)} - \frac{1}{ER_m Bt}\right)M + \frac{u_0(\theta)}{R_m} + \frac{\frac{\partial^2}{\partial\theta^2} u_0(\theta)}{R_m} = 0 \qquad (76).$$

Substituting M (Equation 73) on Equation 76 follows:

$$Hsen(\theta)+\frac{u_0(\theta)}{R_m}+\frac{\frac{\partial^2}{\partial\theta^2}u_0(\theta)}{R_m}=0$$

$$\text{where } H=\left(\frac{ln\left(\frac{R_m+\frac{t}{2}}{R_m-\frac{t}{2}}\right)}{EBt\left(-t+R_m\,ln\left(\frac{R_m+\frac{t}{2}}{R_m-\frac{t}{2}}\right)\right)}-\frac{1}{ER_mBt}\right)\frac{PR_m}{2cos(\beta)} \tag{77}.$$

By solving Equation 77 follows:

$$u=C_1\,cos(\theta)+C_2 sen(\theta)+\frac{H\theta\,cos(\theta)}{2} \tag{78}$$

where C_1 e C_2 are parameters to be determined using the boundary conditions. The boundary conditions are:

$$\begin{cases}\theta=0\Rightarrow u=0\\ \theta=\beta\Rightarrow v=0 \text{ e } -\frac{\frac{\partial u}{\partial\theta}}{R_m}=0\end{cases} \tag{79}.$$

So:

$$\begin{cases}C_1=0\\ C_2=\frac{H}{2}\beta tg(\beta)-\frac{H}{2}\end{cases} \tag{80}.$$

Therefore:

$$\boxed{u=\frac{H}{2}\left(\beta tg(\beta)sen\theta-sen(\theta)+\theta\,cos(\theta)\right)} \tag{81}.$$

Annex 2

Study of the applicability of the data reduction schemes applied on flexural tests of curved beams

A numerical study was performed using the finite element method in order to test the ability of the data reduction schemes described on Section 2.4.2 (ISO 14125 [21] and TCBT) to determine the flexural modulus of curved beams. The numerical study was also used to assess the differences on the results induced by the way the specimen was loaded (concave side up or down).

Numerical model

The value of circumferential modulus claimed by the manufacturer (10.547 GPa) was used as input data in the numerical model. The numerical model supplied new $P-\delta$ curves. The data reduction schemes presented on Section 2.4.2 were applied to the numerical $P-\delta$ curves and new values of circumferential modulus were obtained and compared with the one given by the manufacturer. Thereafter, the ability of the data reduction schemes presented on Section 2.4.2 to calculate the circumferential modulus of the specimens was assessed.

The flexural tests performed on the circumferential specimens were reproduced using isotropic models with 10.547GPa of elasticity modulus. The dimensions of the simulated specimens are given on Table XXV.

Table XXV– Geometrical dimensions of the simulated specimens.

Specimen	t (mm)	B (mm)	L_0 (mm)	L(mm)
Concave side up	12	60	195.9	240
Concave side down	12	60	188.4	240

On Table XXV L_0 is the test span.

The specimens were represented by a finite element mesh with 8400 three-dimensional elements C3D8R defined on Abaqus™ 6.5-1 as depicted in Figure 58.

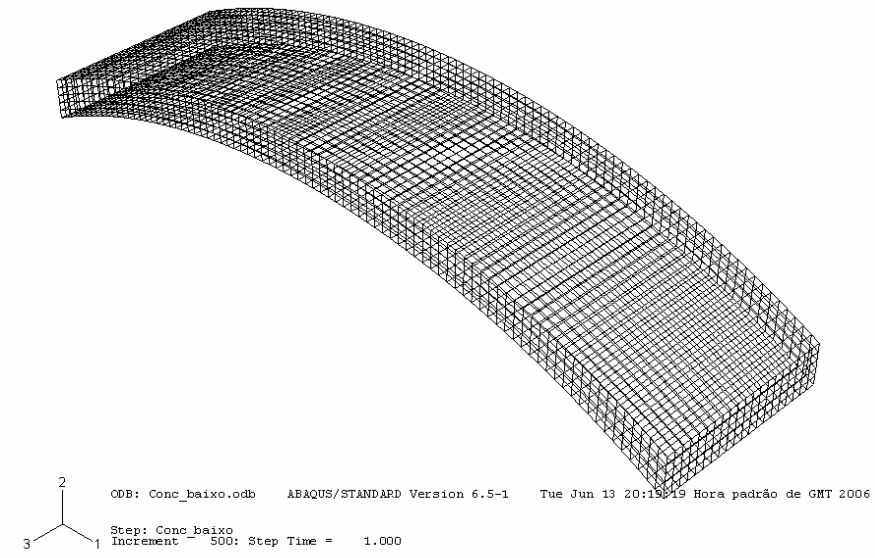

Figure 58 – Finite element mesh.

The boundary conditions reproduce the experimental ones. So, the radial displacements of the specimens on the supports were restricted (Figures 59-60). A displacement of 4mm was applied at mid-span of the specimens using small increments (0.008mm) of displacement. The load and displacement values at the mid-span were acquired at each increment in order to be used on the computations of new values of circumferential modulus.

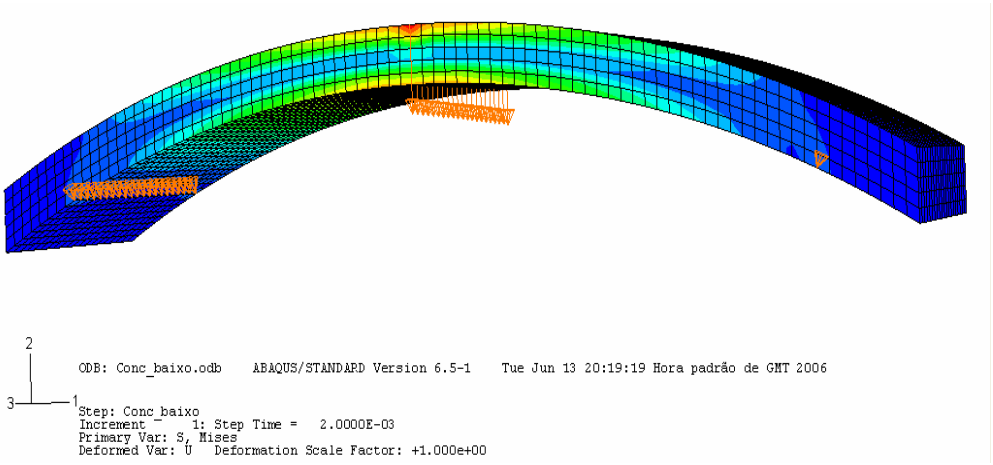

Figure 59 – Specimen simulated with the concave side down.

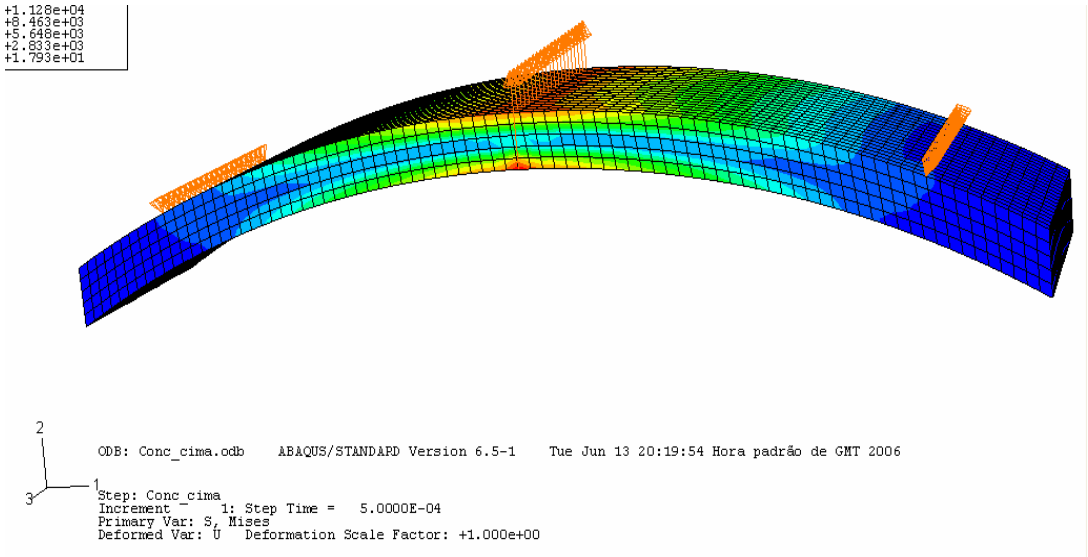

Figure 60 – Simulated specimen with the concave side up.

Numerical results

The obtained numerical $P-\delta$ curves are depicted in Figure 61.

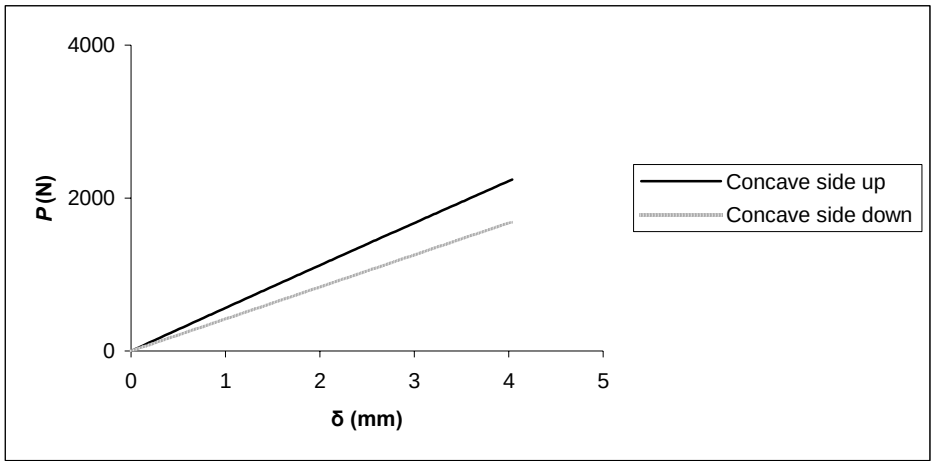

Figure 61 – Numerical $P-\delta$ curves.

The new circumferential modulus obtained numerically is depicted on Table XXVI.

Table XXVI – Circumferential modulus obtained numerically.

Concave side down			
	Slope of the $P-\delta$ curve (N/m)	**E_c (GPa)**	**Error (%)**
ISO 14125	418725	7.573	28.19
TCBT	418725	10.079	4.43
Concave side up			
	Slope of the $P-\delta$ curve (N/m)	**E_c (GPa)**	**Error (%)**
ISO 14125	555770	9.053	14.16
TCBT	555770	10.169	3.98

Discussion of numerical results

The differences between the slopes of the two numerical $P-\delta$ curves are mostly due to the differences of span of the two models.

Through this numerical study of three-point bending tests on curved beams it was seen that the data reduction scheme proposed to linear beams (ISO 14125 [21]) isn't able to be used on the studied curved beams. The obtained error on the circumferential modulus is very high. The thin curved beam theory (TCBT) is able to be applied on the studied curved beams. It is obtained an error of about 4% on the circumferential modulus when this technique is used.